Improved Model for Excess Base Current in Irradiated Lateral PNP Bipolar Junction Transistors

by

Blayne S. Tolleson

A Thesis Presented in Partial Fulfillment
of the Requirements for the Degree
Master of Science

Approved November 2017 by the
Graduate Supervisory Committee:

Hugh J. Barnaby, Chair
Yago Gonzalez-Velo
Jennifer Kitchen

ARIZONA STATE UNIVERSITY

December 2017

ABSTRACT

A modeling platform for predicting total ionizing dose (TID) and dose rate response of commercial commercial-off-the-shelf (COTS) linear bipolar circuits and technologies is introduced. Tasks associated with the modeling platform involve the development of model to predict the excess current response in a bipolar transistor given inputs of interface (N_{IT}) and oxide defects (N_{OT}) which are caused by ionizing radiation exposure. Existing models that attempt to predict this excess base current response are derived and discussed in detail. An improved model is proposed which modifies the existing model and incorporates the impact of charged interface trap defects on radiation-induced excess base current. The improved accuracy of the new model in predicting excess base current response in lateral PNP (LPNP) is then verified with Technology Computer Aided Design (TCAD) simulations. Finally, experimental data and compared with the improved and existing model calculations.

ACKNOWLEDGMENTS

This work was funded in part by the National Aeronautics and Space Administration and the Jet Propulsion Laboratory under contract no. 1562540. The author would like to thank Harald Schone, Mohammad Mojarradi, and Charles Barnes for their support of this work.

TABLE OF CONTENTS

Page

LIST OFTABLES.....v

LIST OF FIGURES.....vi

CHAPTER

1. INTRODUCTION.....1

2. BACKGROUND.....3

2.1. Ionizing-Radiation Modeling Platform for Analog COTS Technology.....3

2.2. Linear Bipolar COTS Components.....4

2.3. Current Gain Degradation.....6

2.4. TCAD Device Modeling.....10

2.5. Interface Trap Formation.....13

2.6. Interface Trap Charge State.....15

3. EXISTING EXCESS BASE CURRENT MODEL.....18

3.1. Space-Charge-Region (SCR) Surface Recombination.....18

3.2. Neutral Base Surface (NBS) Recombination.....24

3.3. Total Excess Base Current Model.....27

4. IMPROVED EXCESS BASE CURRENT MODEL.....29

4.1. Charge State of Interface Traps.....29

4.2. MOS Surface Potential Model Derivation.....32

4.2.1. Lateral PNP Surface Potential Model Modification.....37

4.2.2. Field-Plated Lateral PNP Surface Potential Model Modification....39

4.3 Improved Model Calculations and Simulations.....41

CHAPTER .Page

4.4. Series Resistance Modification.....45

5. EXPERIMETNAL DATA.....49

6. CONCLUSIONS.....57

REFEENCES.....61

LIST OF TABLES

Table Page

1. Constants and Parameters used in Model Calculations and TCAD Device Simulations....48
2. Extracted GLPNP Interface Trap Concentration Data....50
3. Measured GLPNP Excess Base Current Data....51
4. Experimental Excess Base Current and Interface Trap Concentration....52
5. Trapped Oxide Charge Defect Concentrations....55

LIST OF FIGURES

Figure Page

1. Ionizing-Radiation Modeling Platform for Analog COTS Technology.....3

2. Analog Devices AD590 Circuit Schematic and Photomicrograph.....4

3. Texas Instruments LM193 Circuit Schematic.....5

4. Experimental BJT Base Current Data After TID Exposures.....7

5. Experimental BJT Collector Current Data After TID Exposures.....7

6. Experimental BJT Current Gain Data After TID Exposures.....8

7. TCAD Simulated Lateral PNP Base Current.....9

8. TCAD Simulated Lateral PNP Collector Current.....9

9. TCAD Simulated Lateral PNP Current Gain.....10

10. Lateral PNP (LPNP)Transistor TCAD Structure.....11

11. Field-Plated Lateral PNP (FP-LPNP) Transistor TCAD Structure.....12

12. National Semiconductor (NSC) Fabricated LPNP Transistor.....13

13. Acceptor-Like Trap & Donor-Like Trap Energy Distribution.....15

14. Acceptor-Like Trap and Donor-Like Trap Charge State.....16

15. LPNP with Space-Charge Region Surface Defects.....18

16. LPNP with Neutral Base Region Surface Defects.....24

17. Neutral Base Surface Minority Carrier Concentration Profile.....26

18. Charged Interface Traps at the LPNP Base Surface.....29

19. MOS Capacitor Structure.....32

20. LPNP Surface Potential Calculations and TCAD Simulation.....38

21. Field-Plated LPNP (FP-LPNP) Device Cross-Section.....39

Figure Page

22. FP-LPNP Surface Potential Calculation TCAD Simulation.....40

23. LPNP Excess Base Current vs. Emitter-Base Voltage:
TCAD Simulation and Model Calculations.....42

24. FP-LPNP Excess Base Current vs. Emitter-Base Voltage:
TCAD Simulation and Model Calculations.....43

25. LPNP TCAD Simulations with Trapped Oxide Charge.....44

26. LPNP Excess Base Current vs. Emitter-Base Voltage: TCAD Simulation
and Model Calculations with Series Resistance Modification.....45

27. FP-LPNP Excess Base Current vs. Emitter-Base Voltage: TCAD
Simulation and Model Calculations with Series Resistance Modification.....46

28. LPNP Excess Base Current vs Interface Trap Concentration.....47

29. FP-LPNP Excess Base Current vs Interface Trap Concentration.....47

30. National Semiconductor (NSC) Fabricated Gated LPNP (GLPNP) Device.....49

31. GLPNP Extracted Interface Trap Concentration vs. Dose Rate.....50

32. GLPNP Measured Excess Base Current vs. Dose Rate.....51

33. GLPNP Cross-Section.....53

34. Excess Base Current vs. Interface Trap Concentration:
Experimental Data and Model Calculations; Dose Rate of 0.1rad(Si)/s.....54

35. Excess Base Current vs. Interface Trap Concentration:
Experimental Data and Model Calculations; Dose Rate of 20rad(Si)/s.....54

1. INTRODUCTION

The costs associated with implementing linear bipolar commercial-off-the-shelf (COTS) technologies in space-borne systems is driving the need to expand the role of modeling for parts qualification. These costs are primarily associated with the increasing sophistication of next generation systems that require new components not yet qualified and therefore not included on preferred parts lists. Due to the combination of lower cost and greater capabilities of commercial parts, COTS technologies represent an increasing percentage of a system's component inventory. Traditional parts qualification is typically expensive. For lower cost missions, testing every part and technology generation represents a prohibitively high fraction of a mission's budget. One potential solution is the development of effective circuit simulation practices to support "virtual" part qualification.

Developing low cost methods for simulating the total-ionizing-dose (TID) and enhanced-low-dose-rate-sensitivity (ELDRS) response of linear bipolar COTS circuits requires a physics-based model that can predict radiation-induced excess base current (ΔI_B) in a bipolar junction transistor (BJT) to a high level of accuracy. To achieve this, BJT models must accurately reproduce the combined impact of oxide-semiconductor interface traps (N_{IT}) fixed positive oxide trapped charge (N_{OT}). Previous techniques have captured the impact of N_{IT} through the surface recombination velocity (s) parameter and N_{OT} through its impact on depletion width and emitter injection efficiency [1-4]. These older techniques were useful in providing qualitative explanations of the mechanisms of TID effects in BJTs; however, they were limited in their accuracy. A recent paper presented a more qualitatively precise model for radiation-induced excess base current (ΔI_B) [5].

However, the analytical equations models in [5] are still not accurate enough as they do not incorporate the effects of the charged species in the oxide and at the interface. The work presented in this thesis presents refinements to the equations derived in [2, 5]. These refinements focus on capturing the impact of the N_{IT} and N_{OT} charge state on the electrostatic properties of the silicon-oxide layer interface.

To precisely calculate these impacts, metal-oxide-semiconductor (MOS) transistor models are leveraged and applied to predict the surface potential over the base region of a BJT. Although MOS surface potential models are well established in regard to the study and operation of MOS field-effect transistors (MOSFETs), applying such models to predict the physics of radiation-induced excess base current in bipolar transistors, specifically in highly radiation sensitive lateral PNP (LPNP) BJTs, represents a novel approach. One which significantly improves the efficacy of the models described in [2, 5].

2. BACKROUND

2.1. Ionizing-Radiation Modeling Platform for Analog COTS Technology

In an effort to construct an ionizing-radiation modeling platform for analog COTS components and technologies to predict total ionizing dose (TID) and dose rate response of COTS linear bipolar circuits, a modeling framework, shown in Fig 1, has been developed.

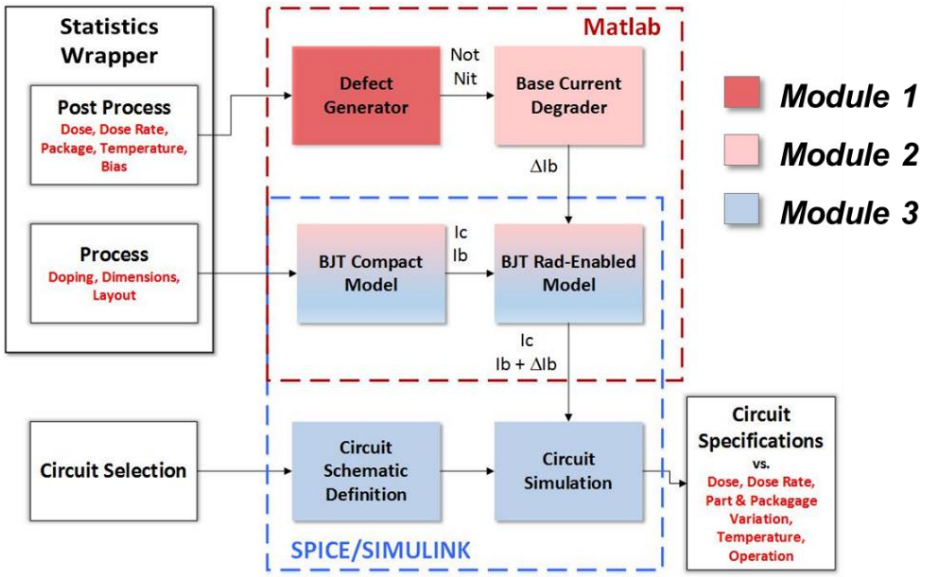

Fig. 1. Framework of ionizing-radiation modeling platform for analog COTS technology.

The framework is divided into three modules, as illustrated in Fig. 1. The first module calculates TID defect buildup at specific doses, dose rates, bias, and thermal conditions. These TID defects are trapped charge in the BJT oxide layer (N_{OT}), and interface traps at the semiconductor-oxide interface (N_{IT}). The second module uses a physics-based analytical model to calculate excess base current in a BJT based on the defect concentrations determined in module 1 and parameterize a radiation-enabled compact model of the transistor. In the third module SPICE simulations of circuits designed using

radiation-enabled BJT models from module 2 are performed to predict component level specification drift in linear bipolar circuits. Depending on circuit type these specifications may include: line regulation, output current, and input bias current as a function of total dose, dose rate, temperature, radiation bias, and even part packaging.

This thesis is focused on the development and refinement of module 2. which is the development of an analytical model to predict the excess current response in a bipolar transistor given inputs of N_{IT} and N_{OT} defects. The thesis will specifically target improvements to the excess base current model for lateral PNP bipolar junction transistors.

2.2. Linear Bipolar COTS Components

Lateral PNP (LPNP) bipolar junction transistors BJTs are used pervasively linear bipolar circuits. Fig. 2 shows the circuit schematic and photomicrograph of the AD590 Temperature Sensor, a commonly used component in space-borne systems [6].

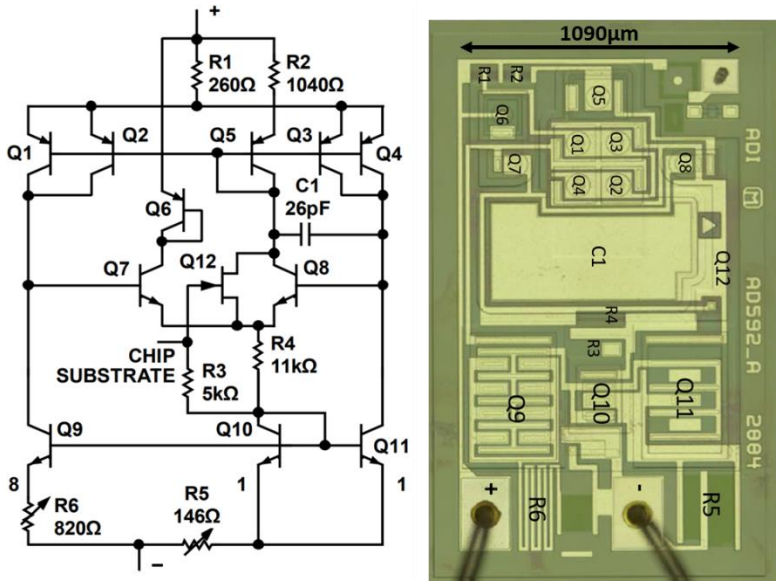

Fig. 2. Analog Devices AD590 temperature sensor circuit schematic (left) and photomicrograph of the IC (right).

The photomicrograph in Fig. 2 reveals two key details: (1) the majority of the PNP transistors in the circuit are LPNP BJTs, and (2) for most of the LPNP devices (i.e., Q1-Q5) there exists a metal field plate over the base oxide layer which is tied to the emitter contact. In fact, the use of emitter-tied field plates over the base region of LPNP transistor is a common layout design practice for many linear bipolar integrated circuit (IC) manufacturers [7]. Barnaby *et al.* described in [7] how an emitter-tied field plate can enhance current gain in LPNP BJT's prior to ionizing radiation exposure.

The field-plated LPNP (FP-LPNP) devices shown in Fig. 2 represents a "gated" type of LPNP structure. However, some linear bipolar COTS components utilize non-gated PNP devices, in which there is only an oxide passivation layer over the base region. In fact, the input transistors of the Texas Instruments LM194 Differential Comparator, also a common component in space-borne systems, are non-gated are substrate PNP transistors [8]. Fig. 3 shows the circuit diagram of the LM193 [9]

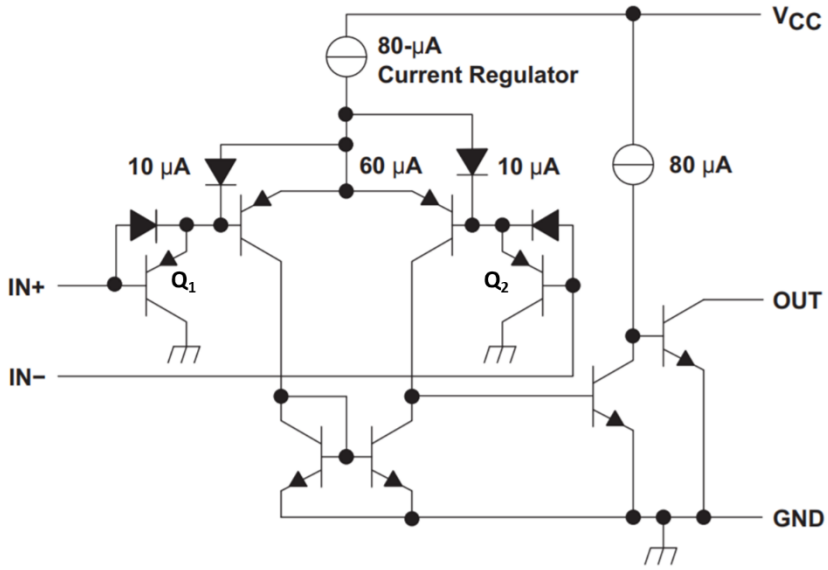

Fig. 3. Texas Instruments LM192 differential comparator circuit diagram; input LPNP transistors are labeled Q_1 and Q_2.

If the circuit in Fig. 3 is exposed to ionizing radiation, excess base current will increase input bias current and degrade the performance of the comparator by decreasing the current gain of the input transistors. This excess base current in PNP BJTs is primarily caused by the buildup of N_{IT} in the bipolar base oxides. [8].

The specific design details of the AD590 and LM193 are not the focus of this thesis. The discussion of these circuit is provided simply to illustrate the extensive use of PNP, particularly lateral, BJTs in commercial components. Considering such a wide-spread usage and high radiation sensitivity, the thesis focuses on the model development of radiation-induced excess base current in LPNPs and FP-LPNP BJT structures.

2.3. Current Gain Degradation

Total ionizing dose (TID) effects cause a significant drop in BJT current gain, which is the ratio of collector (I_C) current to base current (I_B) over a range of emitter-base biases (V_{EB}). This degradation in current gain is chiefly attributed to an increase in base current caused by a radiation-induced buildup of interface traps at the bipolar base semiconductor-oxide (Si–SiO_2) interface [1-5, 8]. Figs. 4 and 5 plot the experimentally obtained BJT base and collector current data prior to (pre-rad) and after TID exposure to 20k, 50k, and 100krad(SiO_2). As the figure shows, TID results in a substantial increase in base current, while the collector current is nearly unchanged. Fig. 6 plots the current gain, $\beta = I_C/I_B$, determined from the experimentally obtained base and collector current data in Fig. 4 and 5.

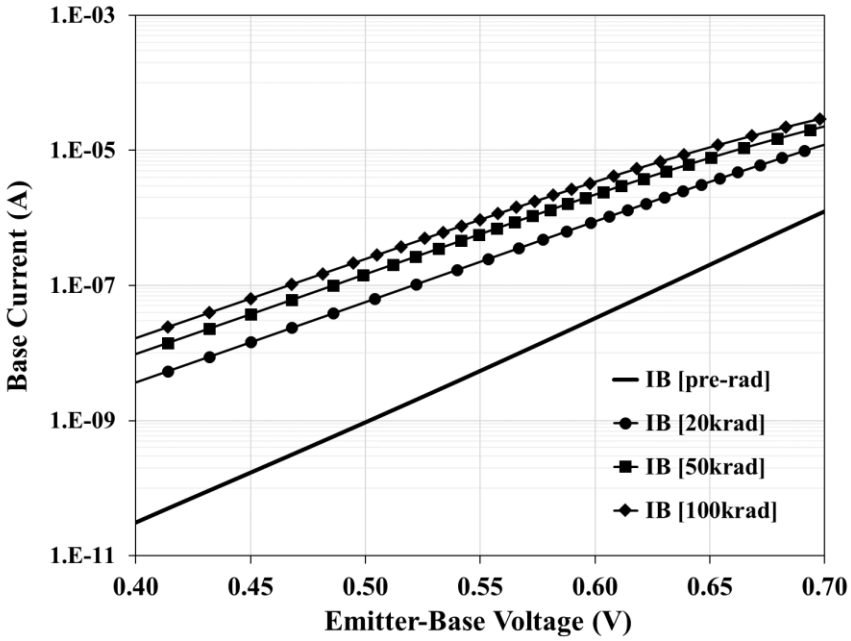

Fig. 4. Experimentally obtained BJT base current vs V_{BE} for TID exposures of 20k, 50k, and 100krad(SiO_2)

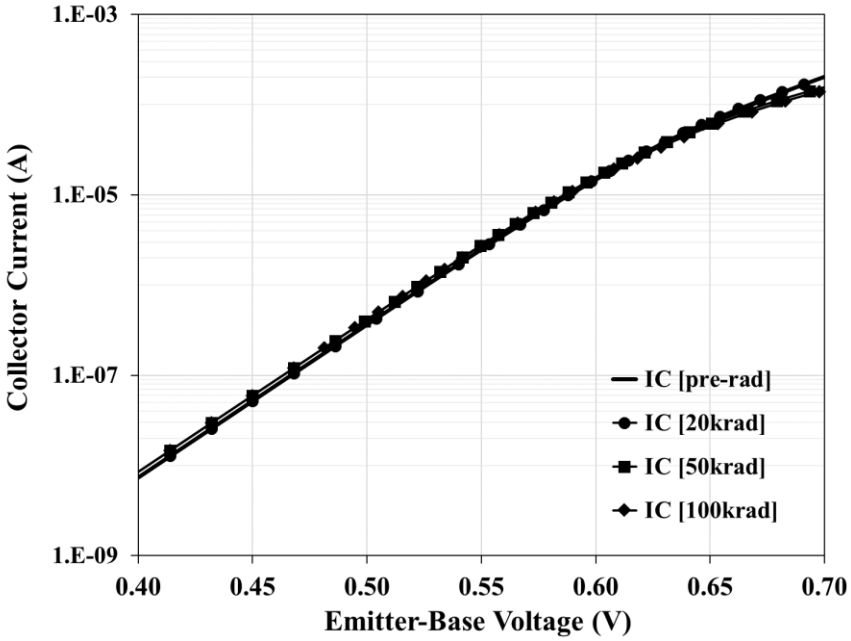

Fig. 5. Experimentally obtained BJT collector current vs V_{BE} for TID exposures of 20k, 50k, and 100krad(SiO_2).

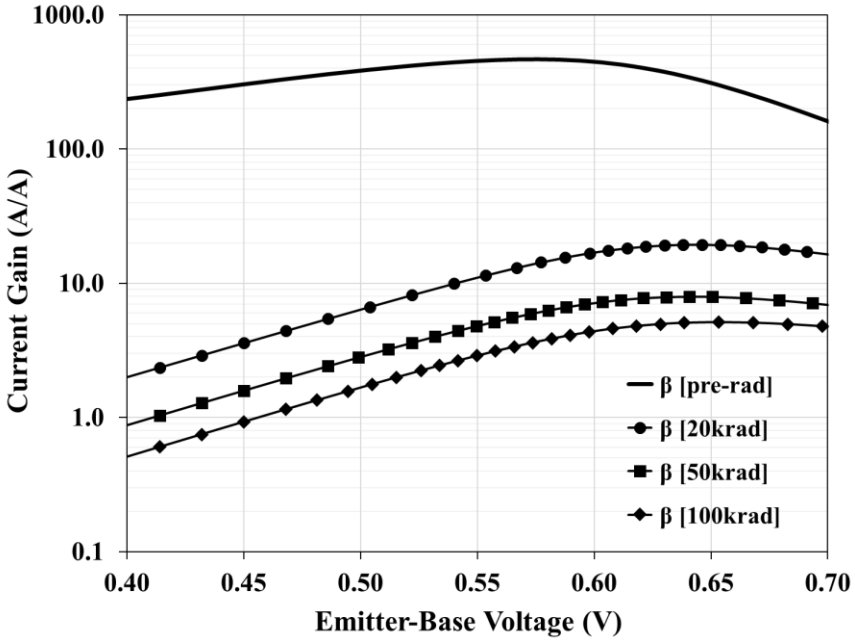

Fig. 6. BJT current gain determined from the base and collector current data in Figs. 4 and 5.

The data in Fig. 6 indicate TID can significantly degrade BJT current gain. In fact, β is decreased nearly two orders of magnitude from pre-irradiated values to values corresponding to a TID of 100krad(SiO_2). Unfortunately, in the experiment used to obtain the data in Fig. 6, the precise Si–SiO_2 interface trap defect concentration resulting from each TID exposure is unknown. Therefore, to justify the claim that the principle cause of current gain degradation in BJTs is the buildup Si–SiO_2 interface traps (N_{IT}), Technology Computer Aided Design (TCAD) simulations were performed with a representative LPNP BJT structure with N_{IT} values ranging from $10^{10}cm^{-2}$ to $10^{11}cm^{-2}$ with trapped oxide charge (N_{OT}) set to 0 cm^{-2}. Figs 7 and 8 plot the TCAD simulated base and collector current vs. emitter-base voltage for this N_{IT} range of values. The simulations in these figures illustrate a similar trend to the experimental data. That is, I_B increases significantly with increasing defect build up, while I_C remains constant.

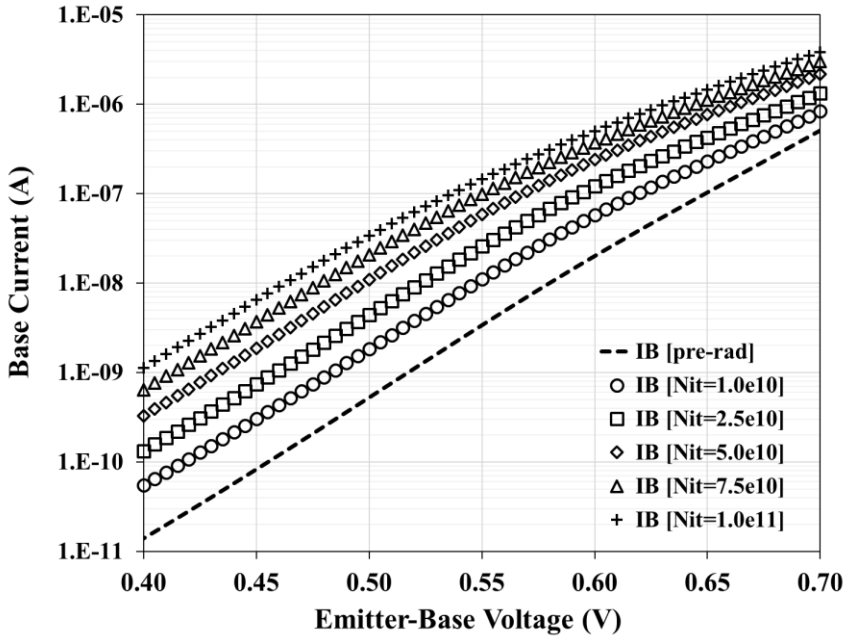

Fig. 7. TCAD simulated LPNP I_B vs. V_{EB} for N_{IT} ranging 10^{10}cm^{-2} to 10^{11}cm^{-2} and N_{OT} = 0 cm^{-2}

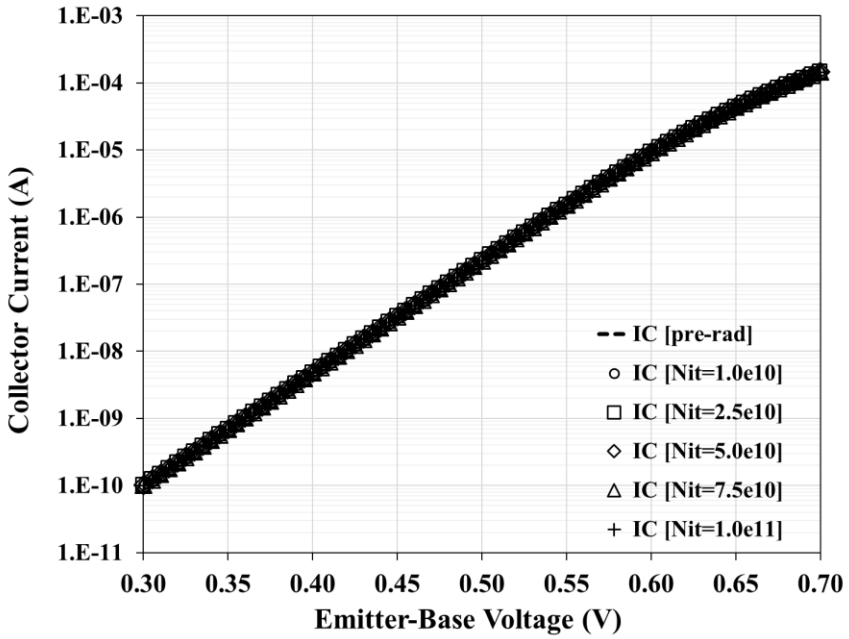

Fig. 8. TCAD simulated LPNP I_C vs. V_{EB} for N_{IT} ranging 10^{10}cm^{-2} to 10^{11}cm^{-2} and N_{OT} = 0 cm^{-2}

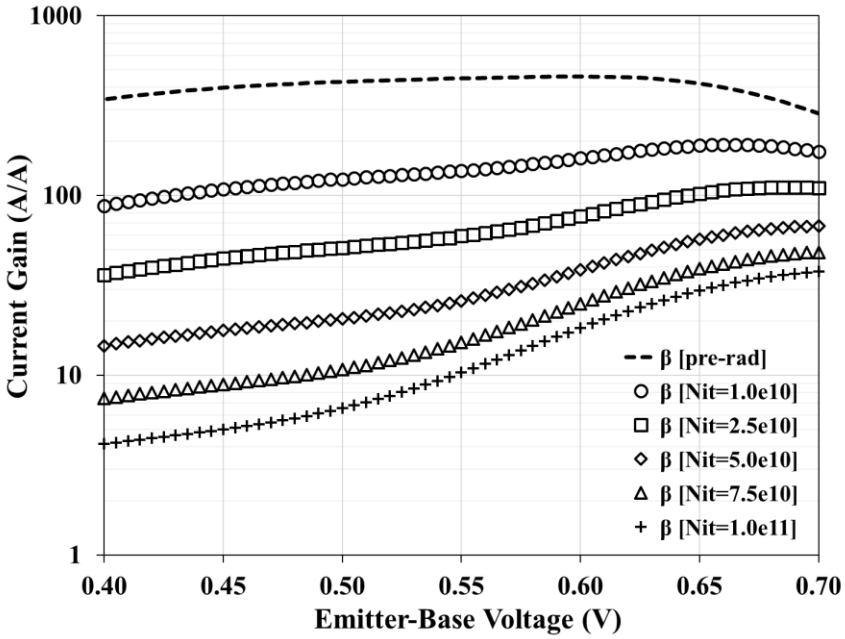

Fig. 9. Current gain determined from the TCAD simulated base and collector currents in Figs. 7 and 8.

In the LPNP TCAD simulations plotted in Figs. 7, 8, and 9, the curves labeled "pre-rad" correspond to $N_{IT} = N_{OT} = 0$ cm^{-2}.

The LPNP TCAD simulation results in Fig. 9 clearly indicate that increasing concentrations of interface traps (N_{IT}) will lead to a severe decrease in transistor current gain. This decrease in current gain can adversely affect the performance of a linear bipolar circuit utilizing LPNP devices.

2.4. TCAD Device Modeling

The technology computer aided design (TCAD) structures used for the above simulations were created and simulated with ATLAS from the SILVACO suite of simulation tools. TCAD is a type of physically-based device modeling technique that can be used to predict the electrical characteristics of specified physical structures over a range

of bias conditions. Physical structures are characterized by dimension, material type, contacts, and impurity (dopant) concentration, and then mapped onto a two or three-dimensional grid, consisting of many grid points, or, nodes. Simulation is carried out via finite element method in which the equations governing semiconductors, i.e. Poisson's equation, Fermi-Dirac statistics, carrier continuity, and carrier transport are numerically solved at each node. Input files are can be used to specify outputs, material parameters, bias conditions, and other features to be used in simulating the structure, as well as the type of simulation (AC, CD, transient, etc.) [11]. Figs. 10 and 11 show the cross-sectional views of the TCAD LPNP and FP-LPNP structures used for device modeling in this thesis.

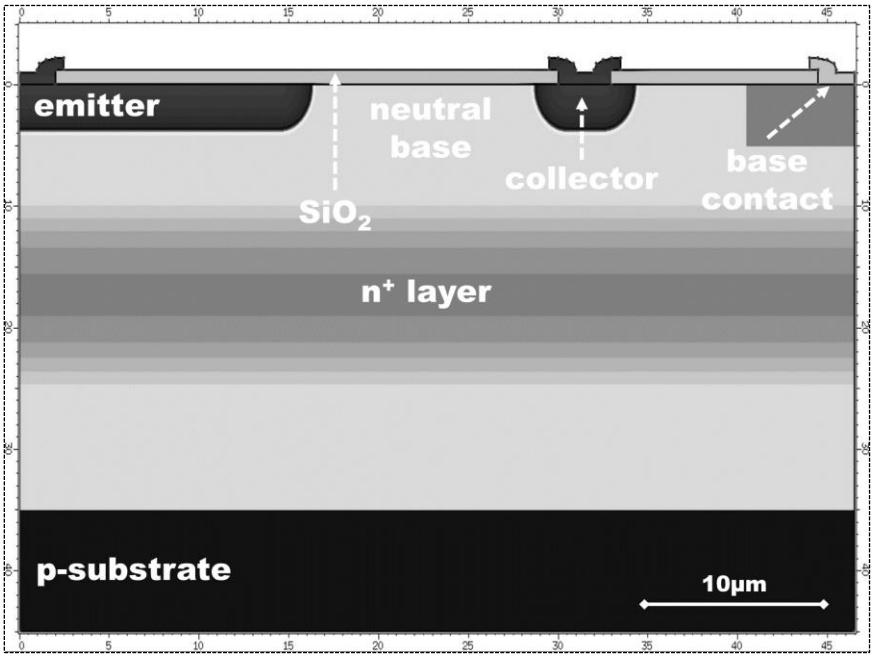

Fig. 10. ATLAS cross-section view of the LPNP TCAD structure used for device simulation.

In the forward bias mode of a PNP transistor, such holes from the highly doped p^+-type emitter are injected into the n-type base and electrons are back injected into the emitter

(I_E). The back-injected electrons constitute the ideal based current (I_B). In a long base structure, minority carrier holes can also recombine with electrons in the base, creating a minority carrier diffusion current. The number of holes that reach the collector, also p^+-type, constitutes the collector current (I_C) [12]. Therefore, current in a PNP BJT can be described by: $I_C = I_E - I_B$.

In the TCAD LPNP structures shown in Figs 10 and 11, an SiO_2 (oxide) layer with a thickness of 1.2 μm is placed over the n-type base. In the simulation input file, the radiation defects of N_{IT} and N_{OT} are place at the Si– SiO_2 interface over the n-type base.

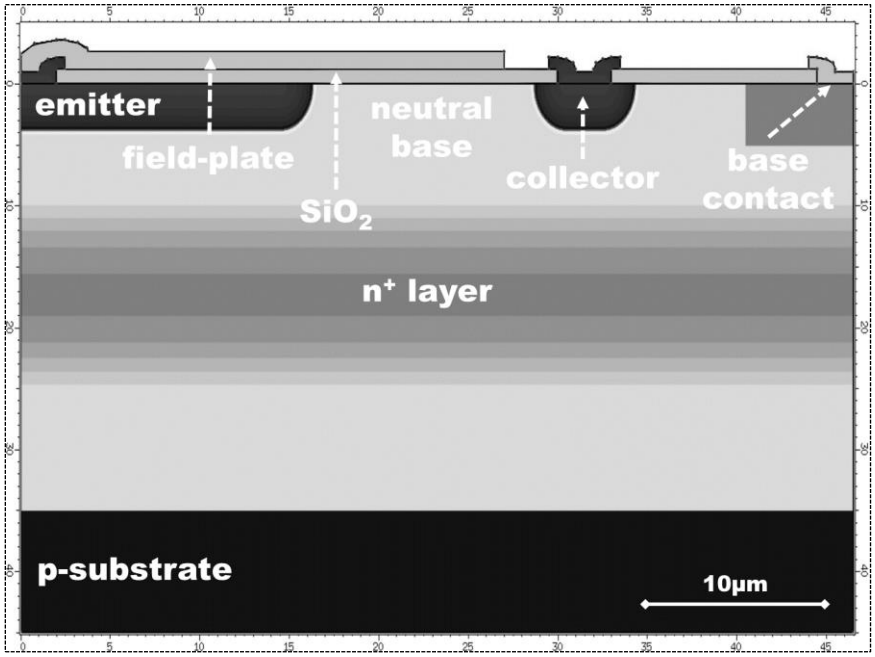

Fig. 11. ATLAS cross-section of the FP-LPNP TCAD structure used for device simulation.

Physically-based device simulation is a valuable tool for numerous reasons. Not only it is far more expedient and cost-effective than conducting experiments on fabricated devices, but it can provide accurate insight and information about device characteristics

that would otherwise be unmeasurable through experimentation. As such, the accuracy of the of the radiation-induced excess base current model for LPNP transistors proposed in this thesis is primarily validated through TCAD device simulations.

These TCAD structures were designed with dimensions, oxide thickness, and doping profiles to mimic devices on LPNP test chips fabricated for the purposes of radiation testing. The LPNP transistors used in these test chips, shown in Fig. 12, were fabricated with the National Semiconductor NSC LM124 process [8]

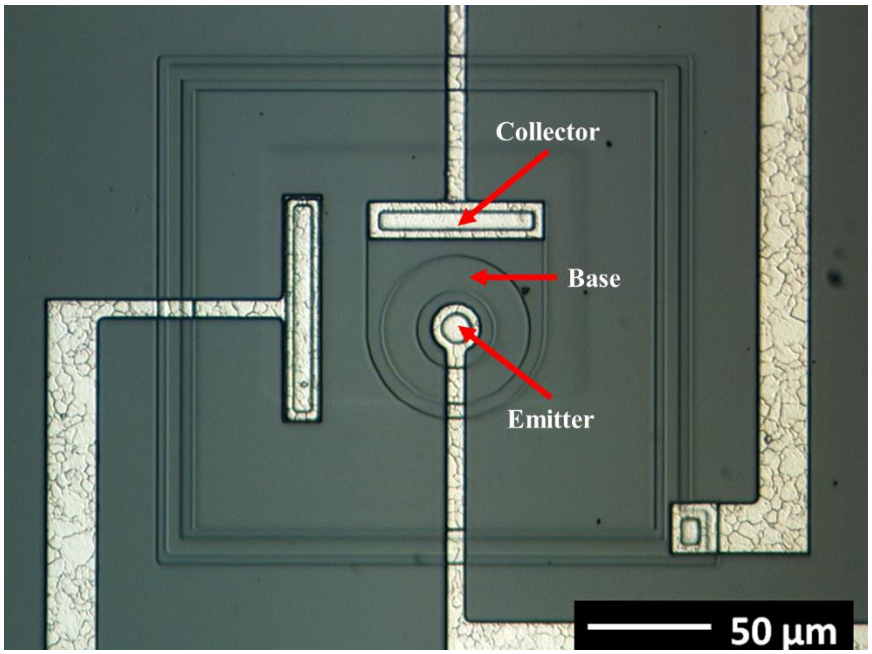

Fig. 12. National Semiconductor Fabricated LPNP transistor

2.5. Interface Trap Formation

In an ionizing radiation environment, a bipolar junction transistor experiences a buildup of defects in the integrated circuit's SiO_2 passivation layer and at the Si–SiO_2 interface above the base region. In a LPNP BJT, defects created in the oxide layer are typically fixed net positive trapped charge per unit area (N_{OT}) and defects created at the Si–

SiO_2 interface are interface traps per unit area (N_{IT}). Prior to radiation exposure both trapped oxide charge and interface trap defect species exist in devices simply as a byproduct of the semiconductor fabrication process [13, 14]. The sophistication of modern fabrication processes typically can keep these defect levels low enough as not to drastically impact the electrical characteristics of the device [13, 14]. Ionizing radiation, however, can significantly increase the number of oxide and interface defects the above pre-irradiation levels. Even in environments with moderate levels of ionizing radiation, this increase in defect concentration can alter the electrical characteristics and performance of certain devices enough to cause circuit failure.

Radiation-induced interface trap formation can occur in two stages: (1) electron-hole pairs are generated in SiO_2 layer as a result of ionizing radiation and the holes react with impurity hydrogen molecules in the SiO_2 layer, thereby releasing protons (H^+) in the oxide; (2) some amount of the protons migrate to the Si–SiO_2 interface and react with the dangling bonds (which have been passivated with hydrogen during processing), thereby de-passivating the bonds, creating interface traps [15, 16]. The mechanisms governing these stages are given by the following reactions between mobile holes (p) and electrons (n), neutral hole-trapping defects (D_A), dangling-bond centers (P_b), and hydrogenated neutral hole trapping defects (D_BH) [Esqueda2012].

Hole-Trapping:

$$D_A + p \rightarrow D_A^+ \qquad \text{reaction (1)}$$

$$D_A^+ + n \rightarrow D_A \qquad \text{reaction (2)}$$

Proton (H^+) Release:

$$D_BH + p \rightarrow D_BH^+ \qquad \text{reaction (3)}$$

$$D_B H^+ \rightarrow D_B + H^+ \qquad \text{reaction (4)}$$

$$D_B H^+ + n \rightarrow D_B \qquad \text{reaction (5)}$$

De-Passivation

$$P_b H + H^+ \rightarrow P_b^+ + H_2 \qquad \text{reaction (6)}$$

In reaction (1) and (2) D_A^+ is a positively charged hole-trapping defect.

2.6. Interface Trap Charge State

Interface traps act recombination-generation (R-G) centers and consist of both "donor-like" traps and "acceptor-like" traps. At the Si–SiO_2 surface interface traps occupying energy levels greater than the intrinsic fermi level, E_i are considered acceptor-like traps, while interface traps occupying energy levels less than E_i are considered donor-like-traps [17]. This differentiation is attributed to the amphoteric nature of interface traps [17]. Each interface trap species can be distributed in energy continuously above and below E_i in the bandgap [18]. Fig. 13 illustrates possible energy level occupancies of donor-like and acceptor like traps.

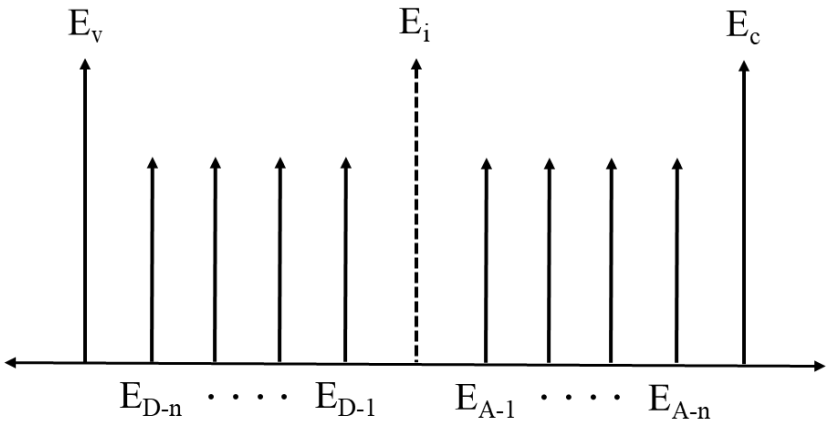

Fig. 13. Possible donor-like and acceptor-like trap energy distribution

In Fig. 13, E_D are the donor-like trap energy levels, and E_A are the acceptor-like trap energy levels. As is common convention, the energy levels E_v and E_c are the valence band and conduction band energy levels, respectively.

Donor-like traps are positively charged when empty and neutral when filled with an electron. Conversely, acceptor-like traps are neutral when empty and negatively charged when filled with an electron, i.e., ionized when filled. This charge state scenario is demonstrated in the energy band diagram shown in Fig. 14.

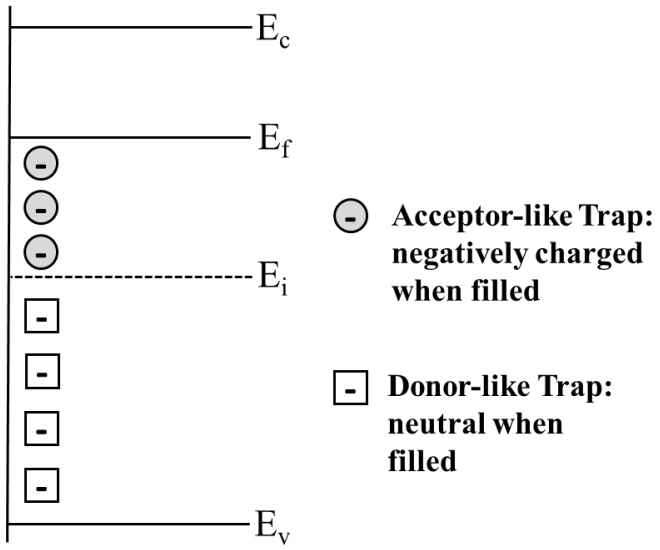

Fig. 14. Charge state of acceptor-like and donor-like interface traps.

Most modeling approaches for TID effects in BJTs only consider interface traps as recombination-generation (R-G) centers that increase surface recombination velocity and do not account for the charge state of N_{IT} [5]. In a PNP, where the base is n-type, most acceptor-like donor-like interface traps will be occupied by an electron. Therefore, it is likely that at base surface N_{IT} will have a net negative charge [17]. This net negative charge

will impact the surface potential and carrier concentration at the bipolar base surface. Furthermore, it is known that surface recombination is dependent on surface carrier concentration. Therefore, developing an accurate model for radiation induced excess base, which is primarily causes by surface recombination at the Si–SiO2 interface [2, 5], the electrostatic impact of charged interface trap defects must be included in the model

3. EXISTING EXCESS BASE CURRENT MODEL

3.1. Space-Charge-Region Surface Recombination Current

Ionizing radiation exposure causes an increase in the number of interface traps (N_{IT}) and trapped oxide charges (N_{OT}) over the entire Si–SiO_2 interface. However, over the portion of this interface located above the emitter-base space-charge region (SCR) the probability of surface carrier recombination via N_{IT} is maximized [4, 10]. Fig. 18 illustrates this defect buildup at the Si–SiO_2 interface above the SCR, where electron-hole pair recombination rate per unit area at the surface increases with N_{IT}.

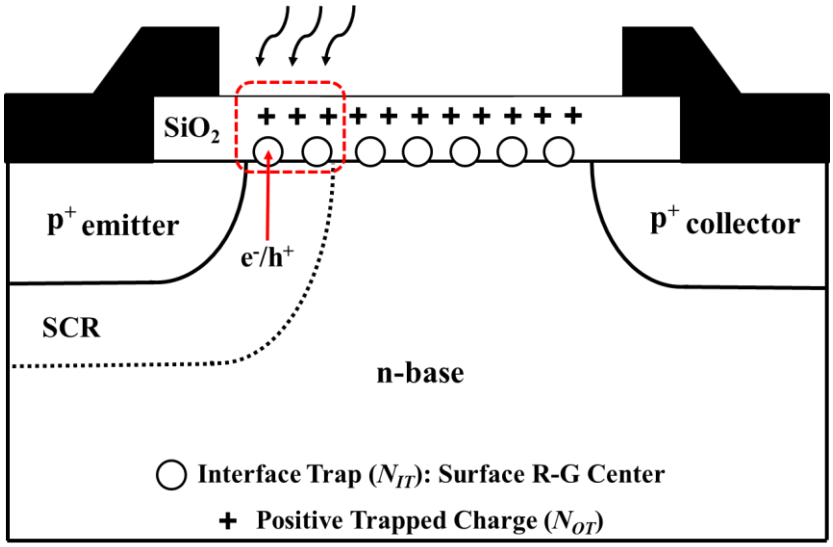

Fig 15. Cross-section of generic LPNP illustrating defect buildup of N_{IT} and N_{OT} over the space charge-region (SCR) surface

At lower positive emitter-base voltages (V_{EB}), typically below 0.5V, recombination in the SCR is the primary contributor to the non-ideal increase in base current [5, 10].

According to Shockley-Read-Hall (SRH) recombination statistics, surface recombination rate (U) can be expressed as

$$U(x) = \Delta s \frac{n(x)\,p(x) - n_i^2}{\left(n(x) + p(x) + 2n_i\right)}, \tag{1}$$

where $n(x)$ and $p(x)$ are the electron and hole concentrations at the Si–SiO2 interface, n_i is the intrinsic carrier concentration of silicon, and Δs is the surface recombination velocity attributed to the increase in interface traps at the Si–SiO2 interface above the SCR [5]. The parameter Δs can be related to the number of interface traps per unit area per unit energy, referred to here as D_{IT}, in the following manner [18]

$$\Delta s = \sigma \upsilon_{th} \int_{E_i - \phi_B}^{E_i + \phi_B} D_{IT}\, dE \simeq 2\phi_B \sigma \upsilon_{th} D_{IT}\,. \tag{2}$$

In Eq. (2), σ is the carrier capture cross-section and υ_{th} is the carrier thermal velocity (~10^7cm/s). The terms ϕ_B and E_i are the bulk potential and intrinsic Fermi energy level. The interface trap concentration N_{IT} can be related to D_{IT} by integrating over the silicon bandgap energy [19], such that

$$N_{IT} = \int_{E_V}^{E_c} D_{IT}\, dE \approx E_g D_{IT}\,, \tag{3}$$

where E_g is the bandgap energy of silicon. It should also be noted that Eqs. (2) and (3) assumes a constant energy distribution of interface traps throughout the Si bandgap [5, 18] and that acceptor-like and donor-like traps are defined above and below the intrinsic Fermi level, respectively [19].

The increase in recombination current at the Si–SiO2 surface above the SCR ($\Delta I_{R\text{-}SCR}$) can be calculated by integrating the SRH recombination rate term in Eq. (1) across the area of the SCR

$$\Delta I_{R-SCR} = q \int_{A_{SCR}} U(x)\, dA = qP_E \int_0^{x_d(V_{EB})} U(x)\, dx \ , \tag{4}$$

where x_d (V_{EB}) is the width of the SCR as a function of emitter-base voltage (V_{EB}), and P_E is the length of the LPNP emitter perimeter [5], and q is magnitude of the elemental charge. In the SCR created by the forward biased emitter-base (p-n) junction, it is a fundamental property that the electron and hole concentrations are related by

$$n(x)\, p(x) = n_i^2 \exp\left(\frac{qV_{EB}}{kT}\right) , \tag{5}$$

where k is Boltzmann's constant and T is device temperature [12]. Eq. (5) is a result of the non-equilibrium expressions describing electron and hole concentrations in a forward-biased junction, which can be expressed as

$$n(x) = n_i \exp\left(\frac{E_{Fn} - E_i(x)}{kT}\right) \tag{6}$$

and

$$p(x) = n_i \exp\left(\frac{E_i(x) - E_{Fp}}{kT}\right) , \tag{7}$$

where E_i (x) is the intrinsic Fermi level; E_{Fn} and E_{Fp} are the quasi Fermi levels for electrons and holes, respectively [12]. If a new variable $\phi(x)$ is introduced where

$$q\phi(x) = E_i(x) - E_{Fp} , \tag{8}$$

then Eqs. (6) and (7) can be re-written as [5]

$$n(x) = n_i \exp\left(\frac{qV_{EB}}{kT} - \frac{q\phi(x)}{kT}\right) \tag{9}$$

and

$$p(x) = n_i \exp\left(\frac{q\phi(x)}{kT}\right), \tag{10}$$

where the split in Fermi levels is related to the applied emitter-base voltage (V_{EB}) by [12]

$$qV_{EB} = E_{Fn} - E_{Fp}\,. \tag{11}$$

The motivation for the substitution described Eq. (8) is that it allows for a closed analytical form of Eq. (1) to be obtained. Using Eqs. (9) and (10), the surface recombination rate described in Eq. (1) can be reformulated as

$$U(x) = \Delta s \frac{n_i \exp\left(\frac{qV_{EB}}{2kT}\right)}{2\cosh\left(\frac{q\phi(x)}{kT} - \frac{qV_{EB}}{2kT}\right)}. \tag{12}$$

From Eq. (4), to calculate the SCR surface recombination current, Eq. (12) must be integrated from x = 0 to x = x_d (V_{EB}); however, the $\phi(x)$ term in the denominator of Eq. (12) is non-linear function in the SCR, which means a closed-form integral of $U(x)$ does not exist [5]. Due sharply peaked shape of recombination in the SCR, it was proposed in [5] by Barnaby *et al* to approximate $\phi(x)$ as a linear function as to allow a closed form evaluation of Eq. (12). With this new linear approximation of $\phi(x)$, which is referred to as $\phi_1(x)$, Eq. (13) becomes $U_1(x)$, where

$$U_1(x) = \Delta s \frac{n_i \exp\left(\frac{qV_{EB}}{2kT}\right)}{2\cosh\left(\frac{q\phi_1(x)}{kT} - \frac{qV_{EB}}{2kT}\right)}. \tag{13}$$

The requirement of $U_1(x)$ is such that

$$U_1(x) \approx U(x) \quad \text{for} \quad x_m - \Delta x \le x \le x_m + \Delta x \tag{14}$$

and

$$\int_{-\infty}^{\infty} U_1(x)\, dx \approx \int_{0}^{x_d(V_{EB})} U(x)\, dx, \tag{15}$$

where Δx is some small distance, and x_m is the location of peak recombination in the SCR [5]. To meet the requirements described in Eqs. (14) and (15), it is proposed by Barnaby *et al* that $\phi_1(x)$ must satisfy the following conditions: $\phi_1(x)$ is linear, $\phi_1(x_m) = \phi(x_m) = V_{EB}/2$, and $d\phi(x_m)/dx = E(x_m)$. Therefore, $\phi_1(x)$ can be formulated as

$$\phi_1(x) = E(x_m)(x - x_m) + \frac{V_{EB}}{2}, \tag{16}$$

where $E(x_m)$ is the x-directional electric field at the point x_m in the SCR, where recombination is at a maximum, i.e., where electron and hole concentrations are equal [5]. In a BJT with a highly asymmetrical junction, where emitter doping is much greater than the base doping, the maximum field can be expressed as

$$E(x_m) = \left[\frac{2qN_D}{\varepsilon_{si}} \left(\frac{kT}{q} \ln\left(\frac{N_D}{n_i} \right) - \frac{V_{EB}}{2} \right) \right]^{\frac{1}{2}}, \tag{17}$$

where ε_{Si} is the permittivity of silicon. The electric field term $E_m(x)$ is also a function of V_{EB} and N_D, the donor concentration of the base [5]. Therefore, Eq. (13) can be rewritten as

$$U_1(x) = \Delta s \frac{n_i \exp\left(\frac{qV_{EB}}{2kT} \right)}{2\cosh\left(\frac{qE_m(x)(x - x_m)}{kT} \right)}. \tag{18}$$

Eq. (18) indicates the maximum electric field term $E(x_m)$ is a critical factor in the SCR surface recombination calculation. Furthermore, the argument of the hyperbolic cosine function is now linear, which allows$U_1(x)$ to be integrated analytically, thus enabling a closed-form expression for the increase in SCR surface recombination current [5]. Using the "linearized" form of $U_1(x)$ described in Eq. (18), Eq. (4) can now be modified as

$$\Delta I_{R-SCR} = qP_E \int_{-\infty}^{\infty} U_1(x)\, dx\,. \tag{19}$$

To calculate the closed integral in Eq. (19), the following identity is used

$$\int_{-\infty}^{\infty} \frac{1}{\cosh(y)}\, dy = \pi\,, \tag{20}$$

with the substitution of variables as follows

$$y = \frac{qE_m}{kT}\left(x - x_m\right) \quad \text{and} \quad dx = \frac{kTE_m}{q}\, dy\,, \tag{21}$$

the analytical expression for the increase in SCR surface recombination current as a caused by ionizing radiation is found to be [5]

$$\Delta I_{R-SCR} = \Delta s \frac{qP_E V_T \pi n_i}{2E(x_m)} \exp\left(\frac{V_{EB}}{2V_T}\right), \tag{22}$$

where $V_T = kT/q$. In Eq. (22), $\Delta I_{R\text{-}SCR}$ is a function of emitter-base voltage V_{EB} and $E(x_m)$ but the only mechanism for increasing surface recombination current in regard to radiation exposure Δs via the increase in radiation-induced defect buildup of N_{IT}.

3.2. Neutral-Base Surface Recombination Current

Ionizing radiation also causes increases in positive trapped oxide charge concentration (N_{OT}) and interface trap concentration (N_{IT}) above the neutral n-type base. As a result, electron-hole recombination along the neutral base surface can increase significantly [2, 4]. Fig. 16 depicts this.

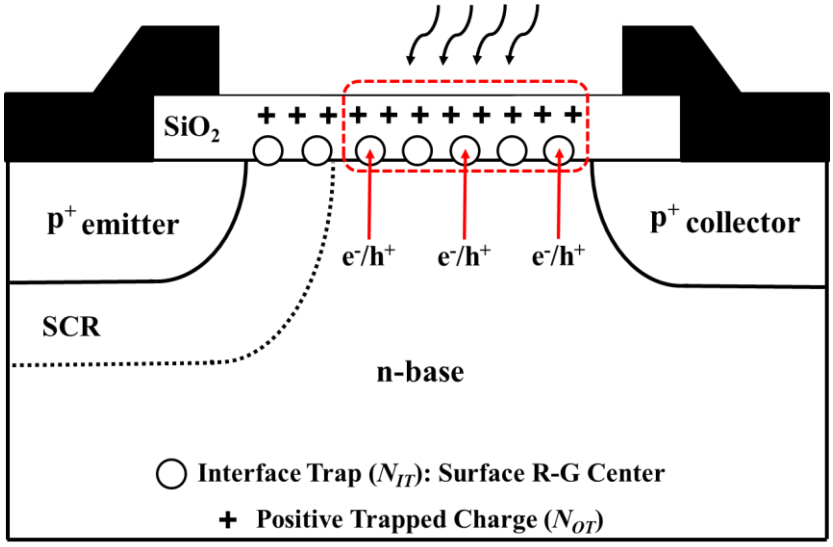

Fig 16. Cross-section of generic LPNP illustrating defect buildup of N_{IT} and N_{OT} over the neutral base surface (NBS).

As in the case of SCR surface recombination, this defect-induced increase in surface recombination along the neutral base surface can lead to an increase in surface recombination current, which in turn further increases the overall base current response of the LPNP transistor [2].

In the emitter-base SCR there is an equal concentration of electrons and holes at the point of maximum recombination. In the neutral base, however, the majority type of carriers are electrons, and the dominant recombination is minority carrier hole

recombination [12]. The excess minority hole concentration (Δp) injected from the emitter as a function distance (x) into the n-type base is given by

$$\Delta p(x) = \frac{n_i^2}{N_D}\left[\exp\left(\frac{V_{EB}}{V_T}\right) - 1\right]\exp\left(-\frac{x}{L_p}\right) \tag{23}$$

where x = 0 is defined as the n-type side the SCR formed by the emitter-base junction, N_D is the base dopant concentration, and L_P is the minority carrier diffusion length [12]. At the Si–SiO2 interface, the excess minority carrier concentration described in Eq. (23) can be modified by replacing the base doping term N_D by the surface electron concentration n_s such that [2]

$$\Delta p_s(x) = \frac{n_i^2}{n_s}\left[\exp\left(\frac{V_{EB}}{V_T}\right) - 1\right]\exp\left(-\frac{x}{L_p}\right) \tag{24}$$

The neutral-base-surface recombination rate (U_s) can therefore be calculated as

$$U_s(x) = \Delta s \Delta p_s(x), \tag{25}$$

where Δs is the same surface recombination velocity term described in Eq. (2). Eq. (25) can then be written as

$$U_s(x) = \Delta s \frac{n_i^2}{n_s}\left[\exp\left(\frac{V_{EB}}{V_T}\right) - 1\right]\exp\left(-\frac{x}{L_p}\right). \tag{26}$$

Furthermore, the neutral base surface recombination current, $\Delta I_{R\text{-}NBS}$, can be calculated integrating $U_S(x)$ over the neutral base surface area (A_{NBS}) as

$$\Delta I_{R-NBS} = q\int_{A_{NBS}} U_s(x)\,dx = qP_E\Delta s\int_0^{W_B}\Delta p_s(x)\,dx\,. \tag{27}$$

where W_B is the width, from emitter to collector, of the base region [2, 12].

For the LPNP structure considered in this work, which is typical of most devices used in linear bipolar COTS circuit technologies, the base width W_B is much smaller than L_P [12]. In this case, the decay of minority carriers outside the SCR is approximately linear with respect to distance x. This is often referred to as the "narrow-base diode" approximation [12]. This linear decay approximation applies to the excess surface minority carrier concentration Δp_s as well [2]. Fig. 14 depicts the linear minority carrier concentration at the base surface.

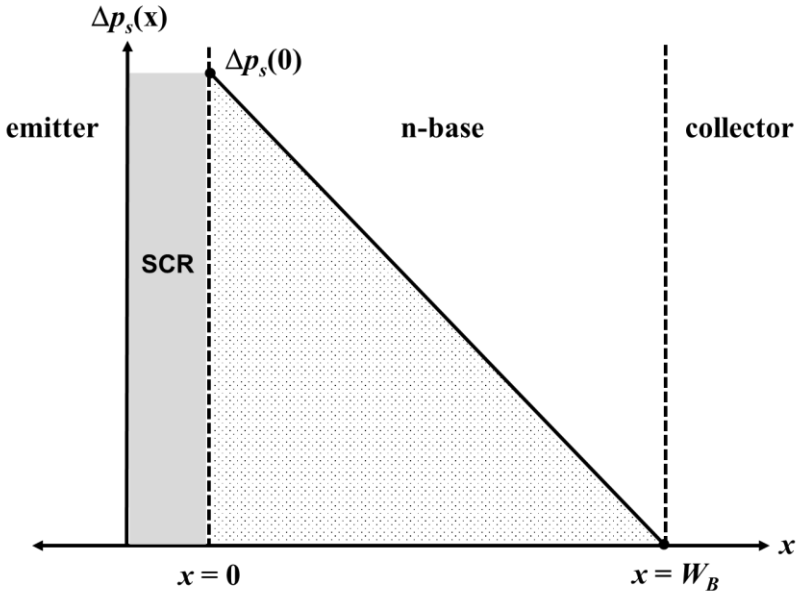

Fig. 17. Minority carrier recombination profile at the neutral base surface

With the narrow-base diode approximation, integrating the excess minority carrier concentration can simply be determined by calculating the area under the curve in Fig. 14, where

$$\int_0^{W_B} \Delta p_s(x)\,dx \cong \frac{1}{2}\Delta p_s(0) W_B . \tag{28}$$

Therefore, the increase in neutral base surface recombination current caused by radiation induced defects

$$\Delta I_{R-NBS} = \Delta s \frac{qP_E W_B n_i^2}{2n_s}\left[\exp\left(\frac{V_{EB}}{V_T}\right)-1\right] \tag{29}$$

Barnaby *et al*., in [2] expressed this current component more accurately as

$$\Delta I_{R-NBS} = \Delta s \frac{qP_E L_P n_i^2}{n_s}\left[\gamma-\gamma\exp\left(\frac{V_{EB}}{V_T}\right)\right] \tag{30}$$

where the function γ is defined by

$$\gamma = \frac{1}{\sinh\left(\frac{W_B}{L_P}\right)} - \frac{1}{\tanh\left(\frac{W_B}{L_P}\right)}. \tag{31}$$

If the scenario exists where $W_B << L_P$, then, using Taylor expansions of hyperbolic functions, (31) simplifies to [12]

$$\gamma = -\frac{W_B}{2L_P}. \tag{32}$$

Substituting Eq. (32) into Eq. (30), yields the same base neutral base surface recombination current expression stated in Eq. (29). In [2] the surface electron concentration n_s in Eq. (30) was assumed to only be a function of positive trapped oxide charge, which leads to a suppression of excess base current by increasing n_s, i.e., surface accumulation.

3.3. Total Excess Base Current Model

The surface recombination currents described in the preceding analysis represent the two current components that make up the total increase in LPNP base current, ΔI_B, resulting from ionizing radiation, meaning

$$\Delta I_B = \Delta I_{R-SCR} + \Delta I_{R-NBS} \,. \tag{33}$$

For an ideal (pre-irradiated) BJT, base current can typically be approximated as

$$I_{pre-rad} = qA\left[\frac{D_n n_i^2}{W_E N_A} + \frac{D_p n_i^2}{W_B N_D}\right]\left[\exp\left(\frac{V_{EB}}{V_T}\right) - 1\right] \tag{34}$$

where A_E is the active emitter area; D_n and D_n are the electron and hole diffusion constants, respectively; N_E and N_B are the p-type emitter and n-type base doping concentrations; W_E and W_B the effective emitter and base widths, respectively [14]. The total base current after radiation exposure is thus modeled as

$$I_B = I_{pre-rad} + \Delta I_B = I_{pre-rad} + \Delta I_{R-SCR} + \Delta I_{R-NBS} \,. \tag{35}$$

4. IMPROVED EXCESS BASE CURRENT MODEL

4.1. Charge State of Interface Traps

Thus far it has been discussed in detail how interface traps (N_{IT}) act as carrier recombination-generation (R-G) centers, thereby increasing surface recombination current via increased surface recombination velocity (Δs). The existing modeling approaches for TID effects in BJTs, however, do not account for the fact that as these recombination centers can be charged. Over the neutral bases, they will typically exhibit a negative charge state [17]. Fig. 18 illustrates this process, where carriers recombine and fill the interface traps, causing the Si–SiO_2 interface to take on a net negative charge if the charged interface trapped density is greater than N_{OT}.

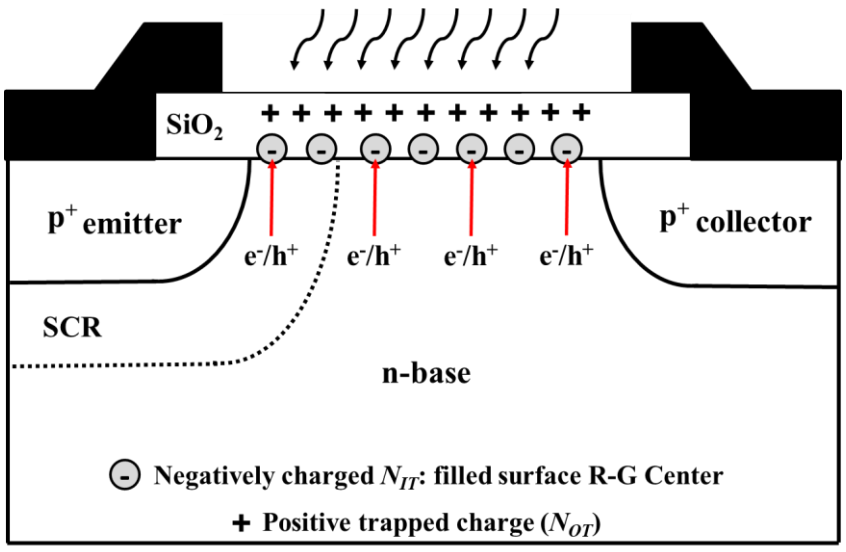

Fig. 18. LPNP cross-section depicting electron-hole pairs filling interface trap R-G resulting in charged N_{IT} at the base surface

To accurately capture the electrostatic impact of charged interface traps on ΔI_B, it is critical to calculate how N_{IT} alters the active base surface potential ψ_s, which was a recognized factor although not included in the model in [2,5].

As previously discussed, the increase in surface recombination current can be found by integrating the SRH recombination over the space charge region surface and neutral base surface area, where

$$\Delta I_{R-SCR} \propto \int_{A_{SCR}} U(x)\, dA \tag{36}$$

and

$$\Delta I_{R-NBS} \propto \int_{A_{NBS}} U(x)\, dA. \tag{37}$$

The SRH recombination term $U(x)$ can be redefined as

$$U(x) \equiv U_s = \Delta s \frac{n_s p_s - n_i^2}{n_s + p_s + 2n_i} \tag{38}$$

where n_s and p_s are the electron and hole concentrations at the LPNP base surface [3], respectively, and are defined as [13]

$$n_s \equiv n(x=0) = N_D \exp\left(\frac{\psi_s}{V_T}\right) \tag{39}$$

and

$$p_s \equiv p(x=0) = \frac{n_i^2}{N_D} \exp\left(-\frac{\psi_s}{V_T}\right). \tag{40}$$

Eqs. (39) and (40) clearly indicate that surface electron and hole concentrations are a function of surface potential ψ_s. Therefore, surface recombination rate, and ultimately ΔI_B, is not only a function of Δs, but also a function of ψ_s.

The existing model for total excess base current ΔI_B described in Eq. (33) was derived using the recombination expressions in Eqs. (36) and (37). However in both models the influence of the N_{IT} charge state on ψ_s was not accounted for. Recall, the ΔI_B model in Eq. (33) is the sum of the space-charge-region surface recombination and neutral base surface recombination currents, $\Delta I_{R\text{-}SCR}$ and $\Delta I_{R\text{-}NBS}$, which are given by

$$\Delta I_{R-SCR} = \Delta s \frac{qP_E V_T \pi n_i}{2E(x_m)} \exp\left(\frac{V_{EB}}{2V_T}\right) \tag{41}$$

where

$$E(x_m) = \left[\frac{2qN_D}{\varepsilon_{si}}\left(\frac{kT}{q}\ln\left(\frac{N_D}{n_i}\right) - \frac{V_{EB}}{2}\right)\right]^{\frac{1}{2}} \tag{42}$$

and

$$\Delta I_{R-NBS} = \Delta s \frac{qP_E W_B n_i^2}{2n_s}\left[\exp\left(\frac{V_{EB}}{V_T}\right) - 1\right]. \tag{43}$$

If the electrostatic impact of the charged interface traps is considered, the base surface electron concentration as a function surface potential $n_s(\psi_s)$ replaces the base doping term in Eq. (42)

$$N_D \rightarrow n_s(\psi_s) = N_D \exp\left(\frac{\psi_s}{V_T}\right). \tag{44}$$

As previously mentioned, the electron concentration term n_s in Eq. (43) was assumed in [2] to be solely a function of positive trapped oxide charge concentration. Therefore, by incorporating the charge impact of N_{IT}, $n_s(\psi_s)$ replace the n_s term in Eq. (43)

$$n_s \rightarrow n_s(\psi_s) = N_D \exp\left(\frac{\psi_s}{V_T}\right). \tag{45}$$

4.2. MOS Surface Potential Model Derivation

To calculate surface potential of the LPNP base region ψ_s, MOSFET surface potential models can be leveraged. Fig. 16 depicts a conventional n-type MOS capacitor structure, mimicking the base region of the LPNP in Fig. 15, which is used to derive the MOSFET surface potential model.

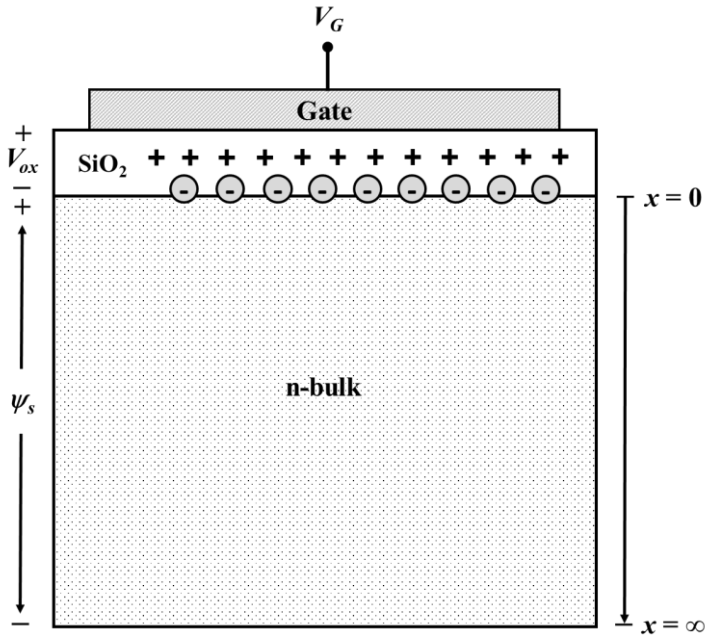

Fig. 19. Typical MOS capacitor structure used for surface potential model derivation.

In the MOS structure in Fig. 16, the voltage applied to the gate is equal to the potential drop across the oxide layer plus the surface potential, such that.

$$V_{GB} = V_{ox} + \psi_s = -\frac{Q_s}{C_{ox}} + \psi_s \tag{46}$$

where V_{GB} is the gate-to-bulk voltage, Q_s is the total charge per unit area induced in the silicon and C_{ox} is the oxide capacitance per unit area, given by [13]

$$C_{ox} = \frac{\varepsilon_{ox}}{t_{ox}} \ . \tag{47}$$

The negative sign attached to the Q_s term in Eq. (42) implies that the charge on the gate is always equal and opposite to the charge in the silicon, meaning that when the V_{GB} is positive, Q_s is negative [13]

In equilibrium, the work-function difference between the gate and the n-type bulk of the MOS capacitor induces charges in the gate and the semiconductor even for a gate-to-bulk bias (V_{GB}) equal to zero. In addition, charges inside the oxide layer and at the oxide-semiconductor interface also induce a semiconductor charge at zero bias. The effect of the contact potential and oxide charges can be counterbalanced by applying a gate-bulk voltage called the flat-band voltage V_{FB} [13]

$$V_{FB} = \phi_{ms} - \phi_{nt} \tag{48}$$

where ϕ_{ms} is the metal-semiconductor work function difference, defined as $\phi_{ms} = \phi_m - \phi_s$, and ϕ_{nt} is the potential related to the charge contribution caused by the radiation defects (N_{IT} and N_{OT}). This radiation induced charge per unit are can be expressed as [13, 14]

$$Q_{nt} = q\left[N_{OT} - \frac{N_{IT}}{E_g}\left(\psi_s + \phi_B\right)\right]. \tag{49}$$

Therefore the radiation-induced defect potential is

$$\phi_{nt} = \frac{q}{C_{ox}}\left[N_{OT} - \frac{N_{IT}}{E_g}\left(\psi_s + \phi_B\right)\right], \tag{50}$$

where the number of interface defects per-unit-area per-unit-energy (D_{IT}) and per unit area (N_{IT}) and are related by normalizing over the bandgap energy, i.e. $D_{IT} = N_{IT}/E_g$.

The gate voltage equation described in Eq. (46) can then be modified to incorporate the effect of V_{FB} [13], where

$$V_G - V_{FB} = -\frac{Q_s}{C_{ox}} + \psi_s \,. \tag{51}$$

Rearranging Eq. (47) yields the following expression

$$V_{GB} - \phi_{ms} + \frac{q}{C_{ox}}\left[N_{OT} - \frac{N_{IT}}{E_g}\left(\psi_s + \phi_B\right)\right] - \psi_s = -\frac{Q_s}{C_{ox}} \tag{52}$$

To derive an expression for the charge Q_s in Eq. (52), Poisson's Equation, which relates potential, electric field, and charge density can be used. Poisson's Equation is

$$\frac{d^2\psi(x)}{dx^2} = -\frac{dE(x)}{dx} = -\frac{\rho(x)}{\varepsilon_{Si}} \,. \tag{53}$$

where $\psi(x)$, is the potential, $E(x)$ is the electric field, and $\rho(x)$ is the charge-density, all as a function of distance x in a given material [13]. The "charge-neutrality" condition for uniformly doped silicon requires that [13]

$$N_D^+ - N_A^- = n(x) - p(x) \,. \tag{54}$$

where N_D^+ and N_A^- are number of ionized donor and acceptor atoms, respectively. Furthermore, for the n-type silicon bulk, $N_A^- = 0$. Therefore, in thermal equilibrium

$$N_D^+ = n_0 - p_0 \,, \tag{55}$$

where n_0 and p_0 are the intrinsic electron and hole concentrations in bulk. The Law of Mass Action states that

$$p_0 n_0 = n_i^2 \,. \tag{56}$$

Solving the system of equations represented by Eqs. (55) and (56), it turns out that

$$N_D^+ = n_0 - p_0 = N_D - \frac{n_i^2}{N_D}. \tag{57}$$

The electron and hole concentrations in the bulk can be written as a function of potential ψ, such that [13]

$$n(\psi) = n_0 \exp\left(\frac{\psi}{V_T}\right) = N_D \exp\left(\frac{\psi}{V_T}\right) \tag{58}$$

$$p(\psi) = p_0 \exp\left(-\frac{\psi}{V_T}\right) = \frac{n_i^2}{N_D} \exp\left(-\frac{\psi}{V_T}\right) \tag{59}$$

With the expressions given in Eqs. (57)-(59), the charge density term ρ can now be expressed as a function of ψ, given by

$$\rho(\psi) = q\left[\frac{n_i^2}{N_D} \exp\left(-\frac{\psi}{V_T}\right) - N_D \exp\left(\frac{\psi}{V_T}\right) + N_D - \frac{n_i^2}{N_D}\right]. \tag{60}$$

Rearranging Eq. (60) yields

$$\rho(\psi) = q\left[\frac{n_i^2}{N_D}\left(\exp\left(-\frac{\psi}{V_T}\right) - 1\right) - N_D\left(\exp\left(\frac{\psi}{V_T}\right) - 1\right)\right]. \tag{61}$$

Using the following property relating the change electric field as a change in potential (ψ) [17]

$$\frac{d^2\psi}{dx^2} = \frac{1}{2}\frac{dE^2(x)}{d\psi}, \tag{62}$$

the electric field $E(x)$ and charge density $\rho(\psi)$ can be related by the following expression

$$\frac{dE^2(x)}{d\psi} = -\frac{2\rho(\psi)}{\varepsilon_{Si}} = -\frac{2qN_D}{\varepsilon_{Si}}\left[\frac{n_i^2}{N_D^2}\left(\exp\left(-\frac{\psi}{V_T}\right) - 1\right) - \left(\exp\left(\frac{\psi}{V_T}\right) - 1\right)\right]. \tag{63}$$

To determine an expression for the electric field, Eq. (63) can be integrated from the bulk ($x = \infty$) to the surface ($x = 0$) with respect to ψ. To calculate this integral, the following boundary conditions are applied: $E(x = \infty) = 0$ and $E(x = 0) = E_s$; $\psi(x = \infty) = 0$ and $\psi(x = 0) = \psi_s$ [13]. Implementing these boundary conditions and integrating Eq. (63) from the bulk to the surface yields the following expression relating the surface electric field E_s in terms of the surface potential ψ_s

$$E_s^2 = \frac{2kTN_D}{\varepsilon_{Si}}\left[\frac{n_i^2}{N_D^2}\left(\exp\left(-\frac{\psi_s}{V_T}\right)+\frac{\psi_s}{V_T}-1\right)-\left(\exp\left(\frac{\psi_s}{V_T}\right)-\frac{\psi_s}{V_T}-1\right)\right]. \tag{64}$$

From Gauss's law, the total charge induced in the silicon at the surface is related to the surface electric field by [13]

$$E_s = \frac{1}{\varepsilon_{Si}}\int \rho(x)\, dx = \frac{Q_s}{\varepsilon_{Si}}. \tag{65}$$

Therefore, using the expression found in Eq. (64), the term Q_s can be calculated as a function of ψ_s by

$$Q_s = \pm\sqrt{2\varepsilon_{Si}kTN_D}\left[\frac{n_i^2}{N_D^2}\left(\exp\left(-\frac{\psi_s}{V_T}\right)+\frac{\psi_s}{V_T}-1\right)-\left(\exp\left(\frac{\psi_s}{V_T}\right)-\frac{\psi_s}{V_T}-1\right)\right]^{\frac{1}{2}}. \tag{66}$$

Substituting Eq. (66) into Eq. (52) provides an expression which defines ψ_s such that

$$\psi_s = V_{GB} - \phi_{ms} + \frac{q}{C_{ox}}\left[N_{OT} - \frac{N_{IT}}{E_g}(\psi_s + \phi_B)\right] - \operatorname{sgn}(\psi_s)\gamma\sqrt{V_T H(\psi_s)} \tag{67}$$

where

$$H(\psi_s) = \left[\frac{n_i^2}{N_D^2}\left(\exp\left(-\frac{\psi_s}{V_T}\right)+\frac{\psi_s}{V_T}-1\right)-\left(\exp\left(\frac{\psi_s}{V_T}\right)-\frac{\psi_s}{V_T}-1\right)\right], \tag{68}$$

and the "body factor" term γ is given by

$$\gamma = \frac{\sqrt{2\varepsilon_{Si} q N_D}}{C_{ox}}. \tag{69}$$

The signum function sgn (ψ_s) in Eq. (67) is defined as being equal to –1 when ψ_s is less than 0V, +1 when ψ_s greater 0V, and equal to 0 when ψ_s is equal to 0V. This function arises from the "±" sign associated with Q_s in Eq. (66), meaning that when the charge induced at the surface is positive the surface potential is also potential, and vice versa.

Given the form of Eq. (67), ψ_s is an implicitly defined function, i.e. a closed-form expression for ψ_s does not exist. Therefore, to obtain particular values of ψ_s, Eq. (67) must be solved iteratively via numerically methods [13]. In this work, the numerical computing environment MATLAB was used to obtain ψ_s values given inputs of N_{IT} and N_{OT}. Closed-form analytical approximations of ψ_s have been proposed in [17, 20, 21] which use non-iterative algorithms to calculate surface potential. This non-iterative approach for calculating ψ_s can eliminate potential convergence issues which may arise in circuit simulators from internal iterative loops. However, this non-iterative method of calculating ψ_s is quite complex and is a study in and of itself. Therefore the ψ_s calculations presented in this paper are found with the MATLAB function "fzero", which uses an iterative algorithm to find the roots of a non-linear function [22]

4.2.1. Lateral PNP Surface Potential Model Modification

The surface potential model in Section 4.2 was derived using the MOS capacitor structure in Fig. 16. For a typical LPNP transistor such as the one depicted in Fig. 15 there is no metal gate over the oxide layer above n-type base region. Without a gate, the gate-to-

bulk voltage V_{GB} and metal-semiconductor work function difference ϕ_{ms} are no longer defined. As a result, the surface potential model in Eq. (67) is modified by setting V_{GB} and ϕ_{ms} equal to 0V.

$$\psi_s = \frac{q}{C_{ox}}\left[N_{OT} - \frac{N_{IT}}{E_g}\left(\psi_s + \phi_B\right)\right] - \mathrm{sgn}\left(\psi_s\right)\gamma\sqrt{V_T H\left(\psi_s\right)} \tag{70}$$

Fig. 20 plots MATLAB calculations of the implicitly defined surface potential ψ_s in Eq. (70). To verify the accuracy of the MATLAB ψ_s calculations surface potential TCAD simulations of the LPNP structure are also plotted in Fig. 20. In both calculation and simulation, N_{IT} is varied from $5\text{x}10^{10}\text{cm}^{-2}$ to $5\text{x}10^{11}\text{cm}^{-2}$with $N_{OT} = 5\text{x}10^{10}\text{cm}^{-2}$.

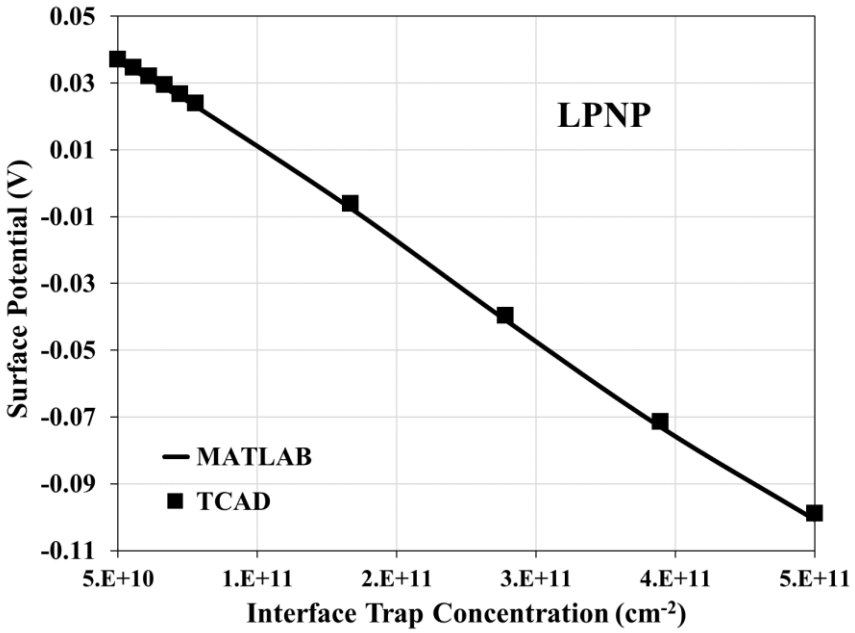

Fig. 20. ψ_s as a function of N_{IT}: MATLAB calculation (solid-line) and TCAD simulation (squares); $N_{OT} = 5\text{x}10^{10}\text{cm}^{-2}$ in both cases.

4.2.2. Field-Plated Lateral PNP Surface Potential Model Modification

Recall linear bipolar COTS components often use LPNP devices with a field-plate over the oxide layer above the base region of the transistor which contacts the emitter-contact. As discussed in chapter 2, the Analog Devices AD590 temperature sensor in Fig. 2 uses these field-plated LPNP (FP-LPNP) devices for the current source transistors in the circuit. Fig. 21 shows an illustration a FP-LPNP device cross-section.

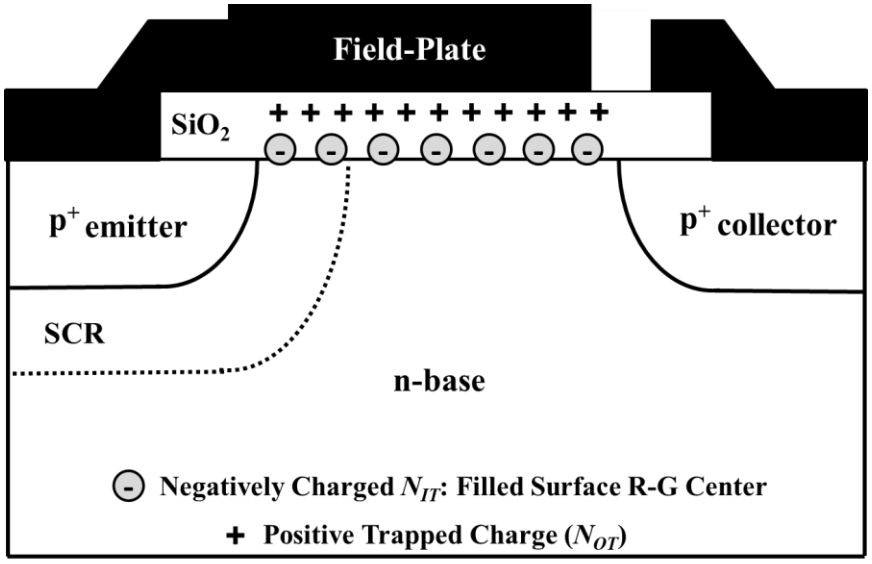

Fig. 21. Field-plated LPNP (FP-LPNP) cross-section.

In the structure in Fig. 21, there is a built-in potential drop (V_{bi}) from the p^+ emitter to the n-type base, or bulk. If the emitter-contact is ohmic, meaning there is no difference between the work function of the emitter and emitter-contact, then ϕ_{ms} = 0V. Since the field-plate Fig. 18 is shorted to the emitter-contact, the gate-to-bulk voltage term in Eq. (67) is modified as

$$V_{GB} = V_E - V_{bi} \tag{71}$$

where V_E is the emitter voltage. Eq. (67) can then be modified as

$$\psi_s = V_E - V_{bi} + \frac{q}{C_{ox}}\left[N_{OT} - \frac{N_{IT}}{E_g}\left(\psi_s + \phi_B\right)\right] - \mathrm{sgn}\left(\psi_s\right)\gamma\sqrt{V_T H\left(\psi_s\right)} \tag{72}$$

where

$$V_{bi} = V_T \ln\left(\frac{N_A N_D}{n_i^2}\right) \tag{73}$$

Eq. (72) indicates that for the FP-LPNP device ψ_s is a function V_E. Fig. 22 plots MATLAB calculations of surface potential ψ_s defined in Eq. (72) and TCAD simulations of the FP-LPNP base surface potential, for emitter voltages of 0V and 0.5V. In all calculations and simulations, N_{IT} is varied from $5x10^{10}cm^{-2}$ to $5x10^{11}cm^{-2}$with N_{OT} = $5x10^{10}cm^{-2}$.

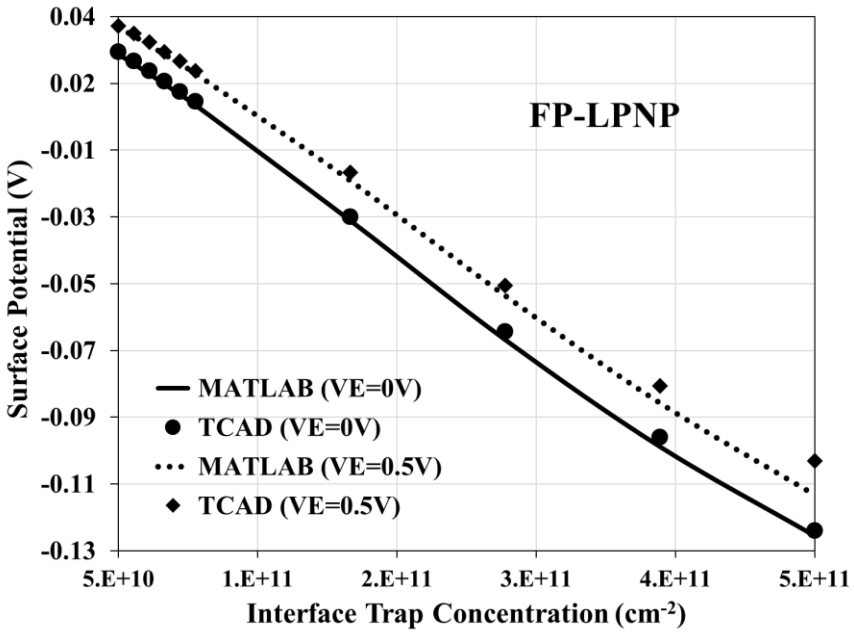

Fig. 22. ψ_s vs. N_{IT}: MATLAB calculation with V_E = 0V (solid-line), V_E = 0.5V (dotted-line) and TCAD simulation simulations with V_E = 0V (black dots), V_E = 0.5V (black diamonds); N_{OT} = $5x10^{10}cm^{-2}$ in all cases.

From the MATLAB calculations and TCAD simulations plotted in Figs. 20 and 22, MOS surface potential models can be leveraged and modified to accurately predict the base surface potential of the LPNP and FP-LPNP structures in Figs. 11 and 12.

4.3. Improved Model Calculations & Simulations

Thus far it has been shown that the charge state of N_{IT} alters the base surface potential which in turn changes the concentration of carriers at the base surface. The surface recombination currents in Eqs. (41) and (43) can be modified to incorporate the surface carrier concentration as a function of surface potential $n_s(\psi_s)$ where

$$\Delta I_{R-SCR}\left(\psi_s\right) = \Delta s \frac{qP_E V_T \pi n_i}{2E\left(n_s\right)} \exp\left(\frac{V_{EB}}{2V_T}\right), \tag{74}$$

$$E\left(n_s\right) = \left[\frac{2qn_s\left(\psi_s\right)}{\varepsilon_{si}}\left(\frac{kT}{q}\ln\left(\frac{n_s\left(\psi_s\right)}{n_i}\right) - \frac{V_{EB}}{2}\right)\right]^{\frac{1}{2}}, \tag{75}$$

and

$$\Delta I_{R-NBS}\left(\psi_s\right) = \Delta s \frac{qP_E W_B n_i^2}{2n_s\left(\psi_s\right)}\left[\exp\left(\frac{V_{EB}}{V_T}\right) - 1\right]. \tag{76}$$

Therefore, the total increase in base current ΔI_B can now be more adequately expressed as a function of ψ_s

$$\Delta I_B\left(\psi_s\right) = \Delta I_{R-SCR}\left(\psi_s\right) + \Delta I_{R-NBS}\left(\psi_s\right). \tag{77}$$

Eq. (77) represents the "improved" model for predicting excess base current in a LPNP BJT caused by ionizing radiation.

Figs. 23 and 24 plot the improved model calculation of excess base current as a function of emitter base voltage. This model uses Eq. (77) calculated with an N_{IT} level of 10^{11}cm^{-2}. Unlike the existing ΔI_B model, also plotted in this figure, the improved model captures the electrostatic effects of the charged interface traps on the surface potential and surface carrier (electron) concentration of the base region, resulting in a significantly closer match to the TCAD simulated LPNP and FP-LPNP structure that uses the same defect levels and device parameters.

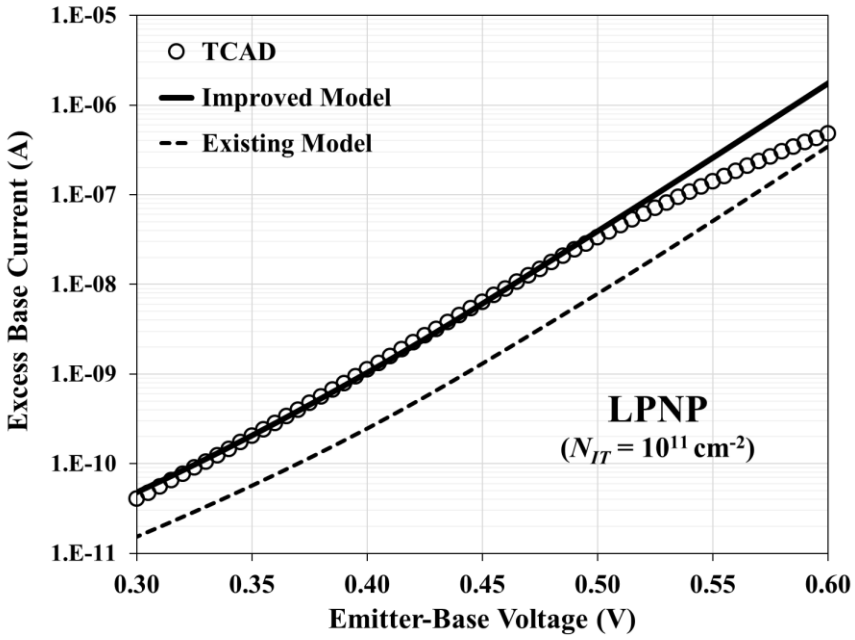

Fig. 23. ΔI_B vs. V_{BE} response of the LPNP TCAD simulation (circles), the improved model calculations (solid-line) and existing model calculations (dashed-line); N_{OT} set to 0cm^{-2}.

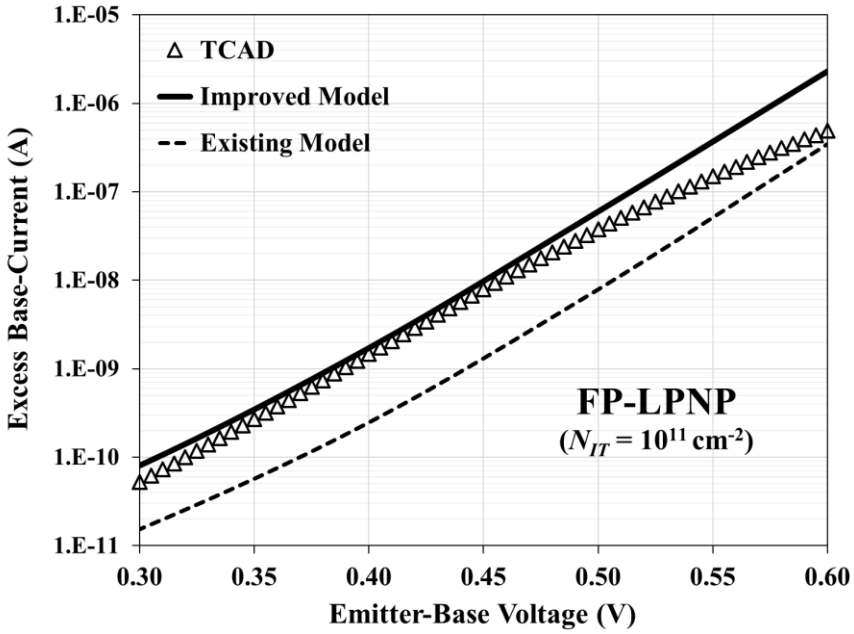

Fig. 24. ΔI_B vs. V_{BE} response of the FP-LPNP TCAD simulation (circles), the improved model calculations (solid-line) and existing model calculations (dashed-line); N_{OT} set to 0 cm^{-2}.

To demonstrate the full effect charged interface traps have on the LPNP excess base current response, the trapped oxide charge defect concentration (N_{OT}) was omitted from the TCAD simulations and model calculations in Fig. 23 and Fig. 24. The motivation for this omission comes the fact N_{OT} represents a positive trapped charge in the oxide layer which counteracts the electrostatic impact of N_{IT} on the surface carrier recombination that causes base current to increase [2]. To illustrate this concept, Fig. 25 plots LPNP TCAD device simulations of total base current as a function of emitter base voltage for a fixed NIT of 10^{11} cm^{-2} and increasing N_{OT} values from 0 cm^{-2} to 10^{11} cm^{-2}.

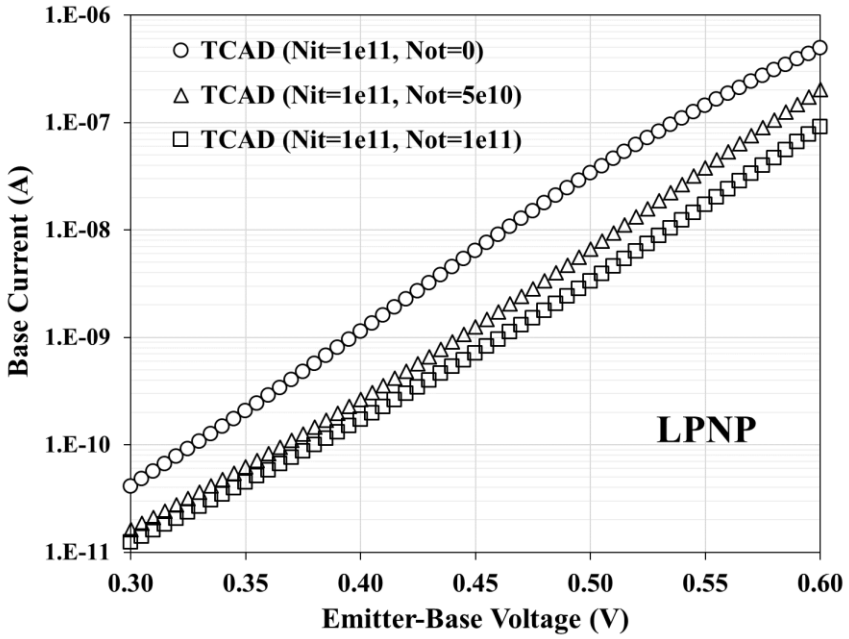

Figure 25. LPNP TCAD total base current simulations: $N_{IT} = N_{OT} = 10^{11}$ cm^{-2} (squares); $N_{IT} = 10^{11}$ cm^{-2} with $N_{OT} = 5x10^{10}$ cm^{-2} (triangles); $N_{IT} = 10^{11}$ cm^{-2} with $N_{OT} = 0$ cm^{-2} (circles)

The TCAD simulations in Fig. 25 clearly indicated that as N_{OT} increases, the overall base current response of the LPNP structure significantly decreases. This further demonstrates the fact that NIT is the primary contributor to excess base current resulting radiation exposure.

4.4. Series Resistance Modification

The TCAD simulations shown in Figs. (23) and (24) show a roll-off in the excess base current response which is attributed to a parasitic series resistance that exists between the emitter and base contacts [12]. As the base current increases, the voltage drop across this series resistor increases, thereby decreasing the effective emitter-base voltage. This

decreases the base current at higher V_{EB} values. This effect can be incorporated into Eqs. (74) and (76) as

$$\Delta I_{R-SCR}(\psi_s) = \Delta s \frac{qP_E V_T \pi n_i}{2E_m(n_s)} \exp\left(\frac{V_{EB} - I_E R_s}{2V_T}\right), \tag{78}$$

and

$$\Delta I_{R-NBS}(\psi_s) = \Delta s \frac{qP_E W_B n_i^2}{2n_s(\psi_s)} \left[\exp\left(\frac{V_{EB} - I_E R_s}{V_T}\right) - 1\right], \tag{79}$$

where I_E is the transistor's emitter current, and R_s is the parasitic series resistance between the emitter and base contacts. As before the total excess base current model is still defined as $\Delta I_B(\psi_s) = \Delta I_{R\text{-}SCR}(\psi_s) + \Delta I_{R\text{-}NBS}(\psi_s)$.

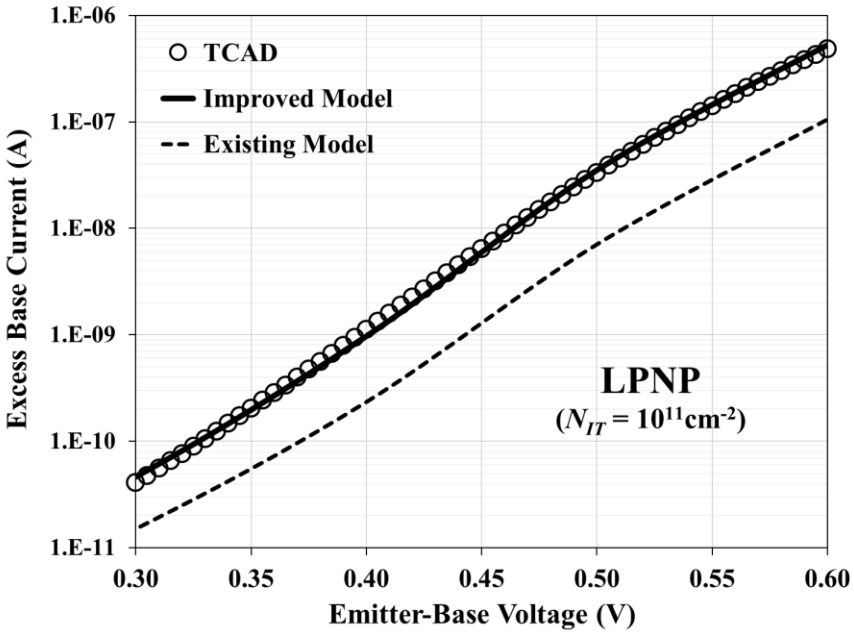

Fig. 26. ΔI_B vs. V_{BE} responses of the LPNP TCAD simulation (circles), the improved model calculations (solid-line) and existing model calculations (dashed-line) with the inclusion of the emitter-to-base series resistance drop; N_{OT} set to 0cm^{-2}.

Figs. 26 and 27 plot the result of incorporating the series resistance drop described in Eqs. (78) and (79) in the excess base current model.

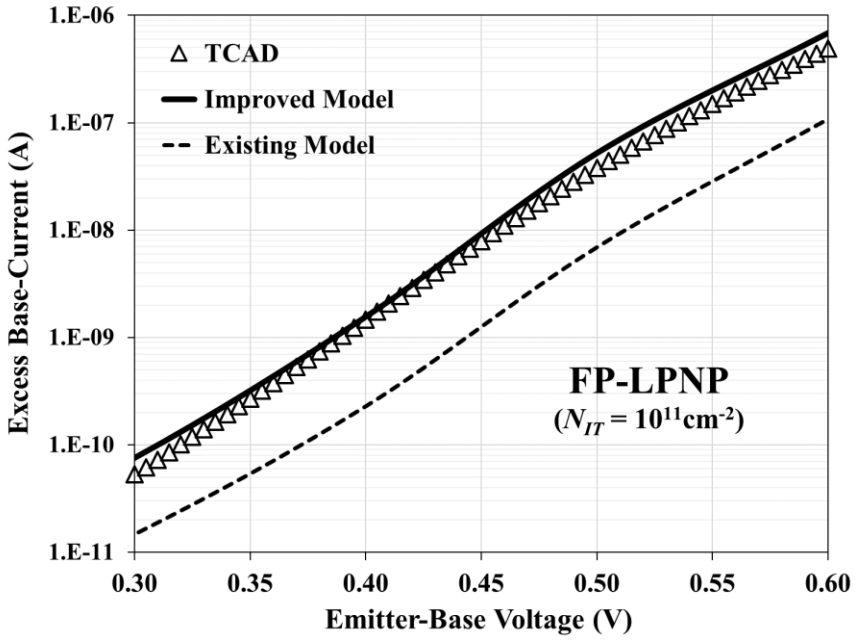

Fig. 27. ΔI_B vs. V_{BE} responses of the FP-LPNP TCAD simulation (circles), the improved model calculations (solid-line) and existing model calculations (dashed-line) with the inclusion of the emitter-to-base series resistance drop; N_{OT} set to 0cm^{-2}.

Demonstrating how the improved model predicts excess base current responses over a range of interface trap concentrations Figs. 28 and 29 plot ΔI_B as function of N_{IT} at a fixed emitter-base voltage of 0.5V. In typical linear bipolar circuit, 0.5V represents a typical transistor low voltage bias point [8]. For each N_{IT} value, the improved model provides a much closer match to the LPNP and FP-LPNP TCAD simulations than the existing excess base current model. For an interface trap concentration of 10^{11}cm^{-2} the existing model calculation is nearly six times lower than the TCAD simulated excess base

current values for both PNP devices. These results demonstrate the improved model's accuracy over a range of N_{IT} levels

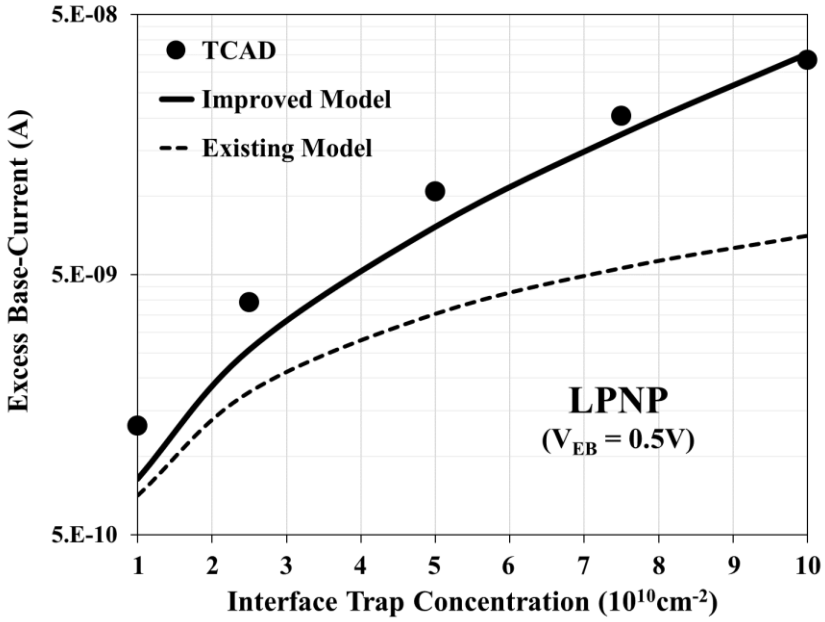

Fig. 28. ΔI_B vs. N_{IT} for LPNP TCAD simulations (solid circles), existing model calculations (dashed-line), and improved model calculations (solid line); all with V_{EB} = 0.5V and N_{OT} set to 0cm^{-2}.

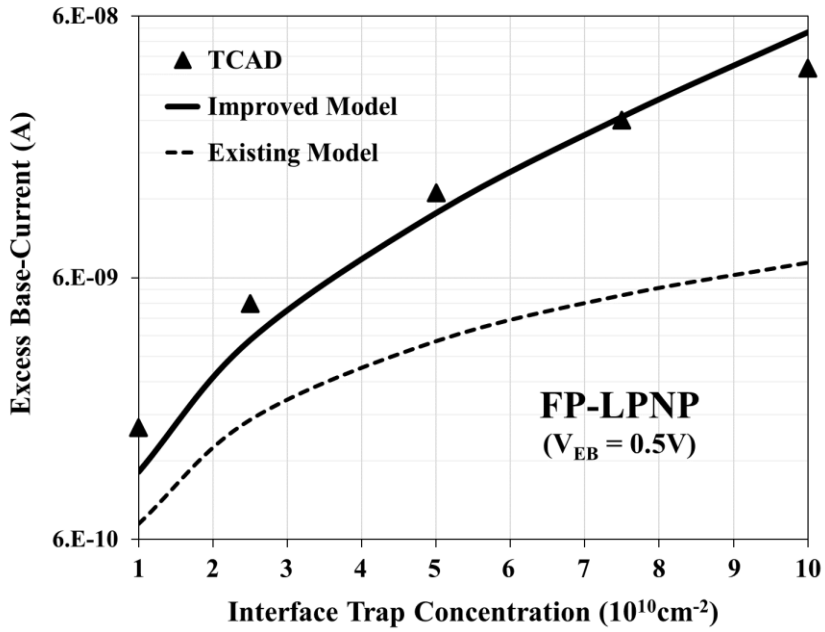

Fig. 29. ΔI_B vs. N_{IT} for FP-LPNP TCAD simulations (solid circles), existing model calculations (dashed-line), and improved model calculations (solid line); all with V_{EB} = 0.5V and N_{OT} set to 0cm^{-2}.

At lower concentrations, the charge contribution from N_{IT} is not as significant as it is at higher concentrations, which means the surface carrier concentration $n_s(\psi_s)$ for low values of N_{IT} is relatively unchanged from the base doping concentration N_D. As a result, the improved ΔI_B model in Figs 28 and 29 shows a better improvement over the existing model as N_{IT} increases.

Table 1. Constants and Parameters used in Model Calculations and TCAD Device Simulations

Symbol	**Parameter**	**Value**	**Units**
V_T	thermal voltage	0.0258	V
ϕ_B	base bulk potential	0.3158	V
V_{bi}	built-in potential	0.810	V
ϕ_{ms}	metal-semiconductor work function diff.	-0.214	V
Eg	Si bandgap energy	1.12	eV
σ	capture cross-section	10^{-15}	cm
υ_{TH}	thermal velocity	10^7	cm/s
q	elementary charge	1.602×10^{-19}	C
ε_{Si}	permittivity of Si	1.04×10^{-12}	F/cm
C_{ox}	Oxide capacitance	2.88×10^{-9}	F/cm^2
n_i	intrinsic carrier conc.	9.89×10^9	cm^{-3}
N_A	emitter doping conc.	2.00×10^{18}	cm^{-3}
N_D	base doping conc.	2.00×10^{15}	cm^{-3}
D_n	electron diffusion coeff.	25.8	cm^2/s
P_E	emitter perimeter	1.036×10^{-2}	cm
W_B	base width	1.20×10^{-3}	cm

5. EXPERIMENTAL DATA

As part of an experiment intended to characterize Enhanced Low Dose Rate Sensitivity (ELDRS) in bipolar transistors, a test chip containing gate lateral PNP (GLPNP) devices was irradiated using the Arizona State University (ASU) Gammacell 220 Cobalt-60 radiation source with dose rates ranging from 0.02rad(Si)/s to 100rad(Si)/s and total doses from 8krad(Si) to 100krad(Si) [8]. The original intent of the experiment was to demonstrate how the amount of hydrogen (H_2) in the device packaging impacts ELDRS and the TID response of linear bipolar circuits. To determine this TID response, N_{IT} values after irradiation were extracted from the GLPNP test chip devices using techniques in [3, 19] for three separate packaging H_2 concentrations; 0.0001% (air), 1.00% and 100% [8]. Fig. 30 shows the fabricated GLPNP transistor used in the experiment.

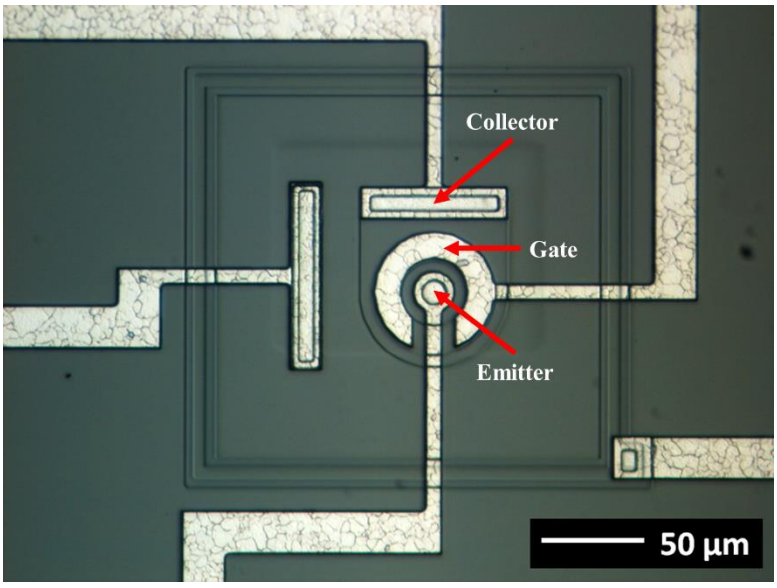

Fig. 30. National Semiconductor (NSC) Fabricated GLPNP device

Fig. 31 plots the extracted GLPNP N_{IT} values as a function of dose rate and the three H_2 concentrations for a total dose of 30krad(Si).

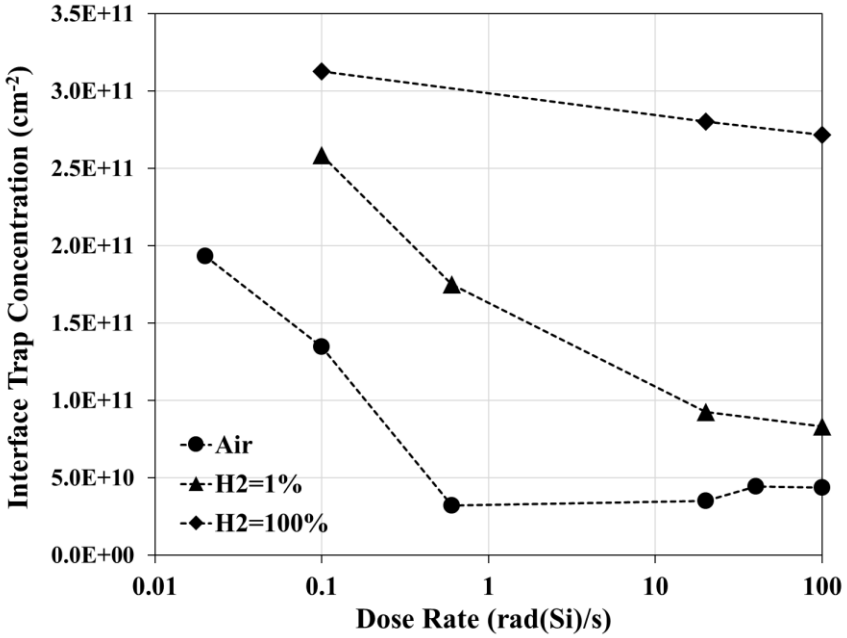

Fig. 31. Extracted GLPNP N_{IT} values vs. dose rate for 30krad(Si) dose.

Table 2. Extracted Interface Trap Concentrations plotted in Fig. 31

Dose Rate (rad(Si)/s)	**N_{IT} (cm^{-2}): Air**	**N_{IT} (cm^{-2}): H2=1%**	**N_{IT} (cm^{-2}): H2=100%**
0.02	$1.94x10^{11}$	-	-
0.1	$1.35x10^{10}$	$2.59x10^{11}$	$3.13x10^{11}$
0.6	$3.22x10^{10}$	$1.75x10^{11}$	-
20	$3.52x10^{10}$	$9.25x10^{10}$	$2.80x10^{11}$
40	$4.44x10^{10}$	-	-
100	$4.37x10^{10}$	$8.34x10^{10}$	$2.72x10^{11}$

Fig. 32 plots the measured GLPNP excess base current after irradiation plotted as a function of dose rate for a TID of 30krad(Si). The data in Fig. 29 was measured with the

HP4156 Semiconductor Parameter Analyzer, with the emitter-base voltage V_{EB} voltage is set 0.5V and the gate voltage V_G set to 0V [8].

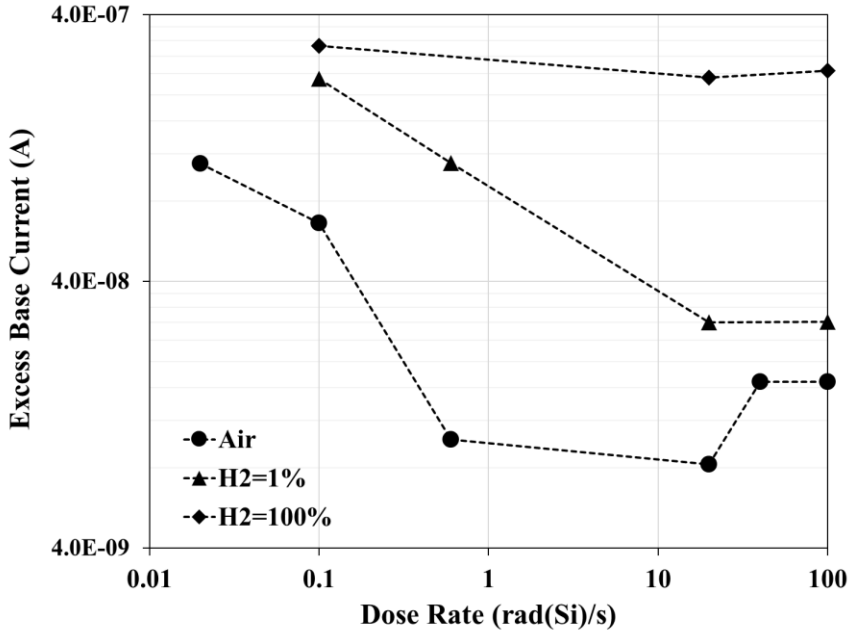

Fig. 32. Measured GLPNP ΔI_B values vs. dose rate for 30krad(Si) dose

Table 3. Measured GLPNP excess base current values plotted in Fig. 32

Dose Rate (rad(Si)/s)	**ΔI_B (A): Air**	**ΔI_B (A): H_2=1%**	**ΔI_B (A): H_2=100%**
0.02	1.11×10^{-7}	-	-
0.1	6.61×10^{-8}	2.30×10^{-7}	3.06×10^{-7}
0.6	1.02×10^{-8}	1.11×10^{-7}	-
20	8.23×10^{-9}	2.81×10^{-8}	2.33×10^{-7}
40	1.68×10^{-8}	-	-
100	1.68×10^{-8}	2.81×10^{-8}	2.46×10^{-7}

The experimental data shown in Figs. 31 and 32 indicates the amount external hydrogen in the environment surrounding the device strongly impacts the ELDRS parameter known as the low dose rate enhancement factor, which is roughly defined as

ratio of base current degradation (increase) at a low dose rate to the base current degradation at a high dose rate, for a fixed total dose [8, 16, 23]. The experimental data also illustrates that as H_2 concentration increases, the maximum degradation, i.e. interface trap concentration, at low dose rates increases [8].

Although the effect of hydrogen on low dose rate enhancement factor is important in understanding total dose and dose rate responses of linear bipolar circuits, it is not the focus of this thesis. The data in Table 2 and Table 3 however can be used to gathe experimentally obtained ΔI_B as a function of N_{IT}. Table 4 contains the GLPNP extracted N_{IT} and measured ΔI_B data at dose rates 0.1rad(Si)/s 20rad(Si)/s a TID of 30krad.

Table 4. Experimental GLPNP ΔI_B and extracted N_{IT} values.

Dose Rate (rad(Si)/s)	**Dose (krad(Si))**	**H_2%**	**V_{EB} (V)**	**V_G (V)**	**N_{IT} (cm^{-2})**	**ΔI_B (A)**
0.1	30	0.0001%	0.5	0	$1.35x10^{11}$	$6.61x10^{-8}$
0.1	30	1.00%	0.5	0	$2.59x10^{11}$	$2.30x10^{-7}$
0.1	30	100%	0.5	0	$3.13x10^{11}$	$3.06x10^{-7}$
20	30	0.0001%	0.5	0	$3.52x10^{10}$	$8.23x10^{-9}$
20	30	1.00%	0.5	0	$9.25x10^{10}$	$2.81x10^{-8}$
20	30	100%	0.5	0	$2.80x10^{11}$	$2.33x10^{-7}$

To test the improved excess base current model's ability to predict experimental results, the V_{EB}, V_G, and N_{IT} data in Table 4 can be used as inputs to produce model calculations of ΔI_B and compared to the measured ΔI_B of the irradiated GLPNP device. Since the irradiated device in Fig. 30 is gated lateral PNP, the improved model uses the surface potential calculated given by

$$\psi_s = V_{GB} - \phi_{ms} + \frac{q}{C_{ox}}\left[N_{OT} - \frac{N_{IT}}{E_g}\left(\psi_s + \phi_B\right)\right] - \mathrm{sgn}\left(\psi_s\right)\gamma\sqrt{V_T H\left(\psi_s\right)} \qquad (80)$$

Excess base current measurements taken on the test chip GLPNP devices were taken with the gate voltage set to 0V; therefore V_{GB} = 0V in Eq. (80). In surface potential calculation, the metal work function is set to that of aluminum: ϕ_m = 4.08eV. Aluminum is typically used to make contacts in devices like the GLPNP in Fig 30. The cross section of a GLPNP is depicted in Fig. 33

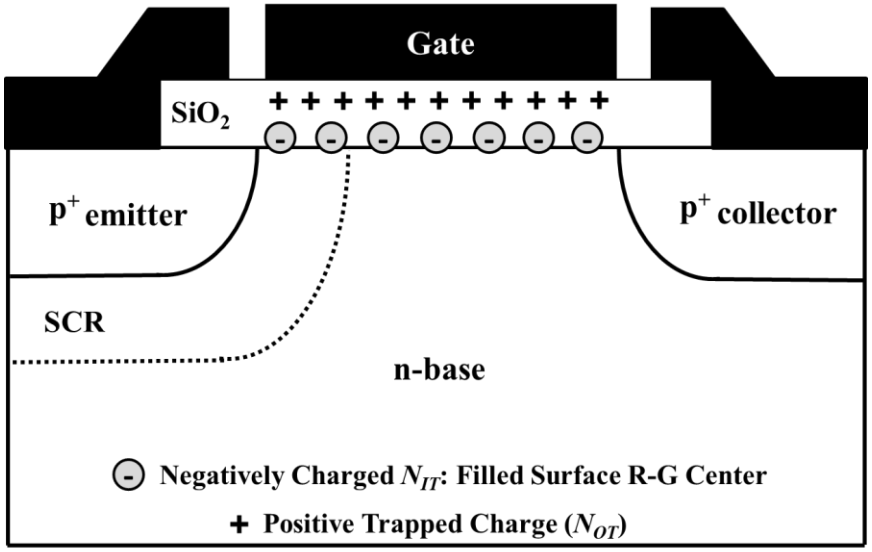

Fig. 33. Cross-section of a gated LPNP (GLPNP)

Fig. 34 plots the experimentally obtained excess base current data as well as the improved model and existing model calculations of excess base current for the N_{IT} values corresponding 0.1mrad(Si)/s dose rate (DR) rows in Table 4. Fig 35 plots the same data and model calculations corresponding to the 20mrad(Si)/s dose rate rows in Table 4.

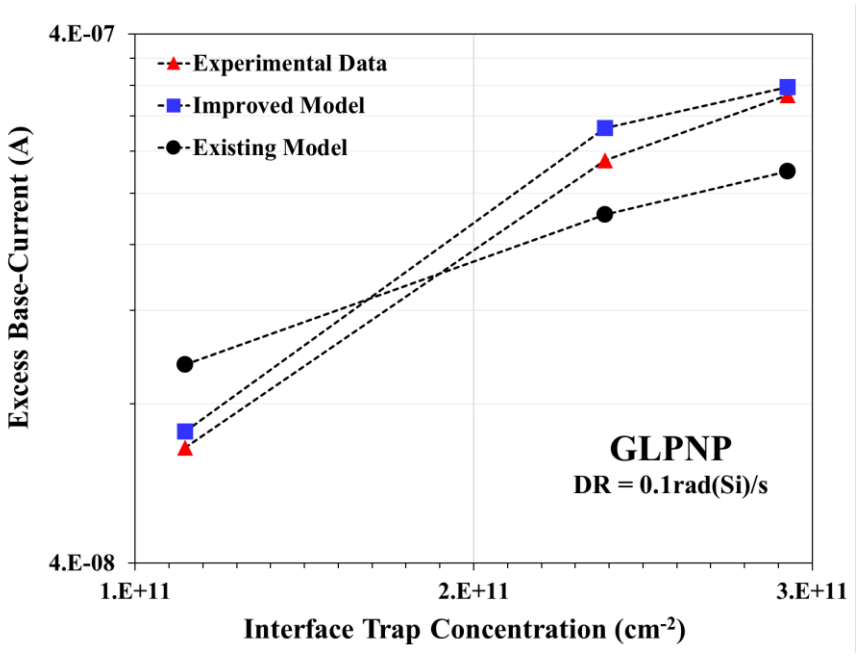

Fig. 34. Experimental ΔI_B data (triangles), ΔI_B calculated with improved model (squares) and ΔI_B and calculated with existing model (dots) for 0.1mrad(Si)/s data in Table 4.

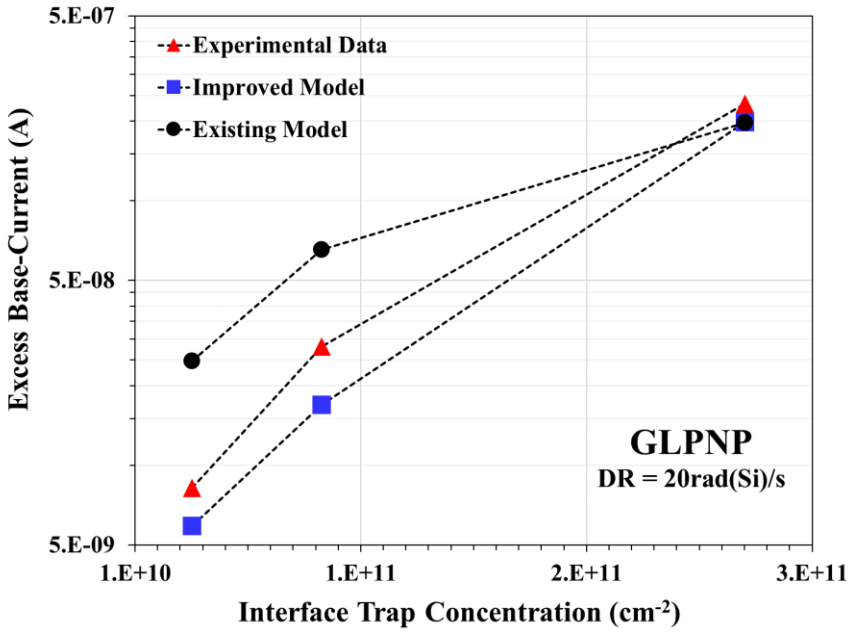

Fig. 35. Experimental ΔI_B data (triangles), ΔI_B calculated with improved model (squares) and ΔI_B and calculated with existing model (dots) for 0.1mrad(Si)/s data in Table 4.

In the experiment conducted the to obtain the data in Table 4, the trapped oxide charge defect concentration (N_{OT}) was not measured. Unlike in model verification via TCAD simulation, the existence of N_{OT} cannot be ignored. Given information in [3], the N_{OT} values use in the improved and existing model ΔI_B calculations in Figs. 34 and 35 are given in Table 5.

Table 5. N_{OT} values used for model calculations in Figs. 31 and 32

Dose Rate (rad(Si)/s)	**Dose (krad(Si))**	**N_{IT} (cm^{-2})**	**N_{OT} (cm^{-2})**
0.1	30	$1.35x10^{11}$	$4.50x10^{10}$
0.1	30	$2.59x10^{11}$	$6.00x10^{10}$
0.1	30	$3.13x10^{11}$	$7.50x10^{10}$
20	30	$3.52x10^{10}$	$4.50x10^{10}$
20	30	$9.25x10^{10}$	$6.00x10^{10}$
20	30	$2.80x10^{11}$	$7.50x10^{10}$

In Table 5 the same range of N_{OT} values were used in the ΔI_B model calculations for 0.1mrad(Si)/s and 20mrad(Si)/s. In [3] it is determined that N_{OT} shows minimal change with dose rate.

Figs. 34 and 35 indicate that the improved model more closely matches the experimental data than the existing model. In Fig. 34 the improved model calculation slightly over estimates the experimental data at the lower N_{IT} levels, but aligns very closely to the data at the largest N_{IT}. In Fig. 35 the improved model calculations align more to the

measured data at the two lower N_{IT} values, and both models and measured data seem to be approximately that same at the largest value of $N_{IT.}$

The general trend in both figures is that the improved model calculation more adequately predicts the excess base current of the irradiated GLPNP. This further demonstrates improvements of the model over the existing model.

6. CONCLUSIONS

Bipolar transistors play a variety of important roles in systems where they are exposed to ionizing radiation. Because of their low cost and high gain-bandwidth product compared to MOSFET transistors they are used extensively for analog circuits utilized in spaceborne applications. In such environments, exposure to ionizing radiation causes a significant increase in bipolar base current, which reduces current gain and can cause component specifications like output current, input bias current, or voltage regulation to drift from nominal levels. If this drift is severe enough, system failure can occur. As such, to have a physics-base analytical model to accurately predict base current degradation would allow designers to create more reliable systems.

Existing models for the radiation-induced increase, or “excess”, base current in LPNP devices were introduced and analyzed thoroughly. These models describe the radiation-induced increase in bipolar base current resulting from increased surface recombination at the semiconductor-oxide interface above the LPNP emitter-base space charge region and neutral base region brought on by a buildup of radiation induced interface traps. This results in increased surface recombination velocity. Although surface recombination remains a critical component in calculating base current responses brought about by ionizing radiation, the existing models fail to account for the electrostatic properties of these interface traps.

Like other types of trap defects, such as ones created in the bulk silicon, interface traps act as carrier recombination centers. However, these radiation-induced traps created at the silicon-oxide interface can exist at any energy level within the silicon bandgap. Because of this distinguishing characteristic, interface traps can contribute negative charge

to surface of LPNP base region [17, 18]. As interface trap concentration increases with radiation exposure more and more negative charge is contributed, which in turn changes the electrostatic properties of the base surface, namely the surface carrier concentration. The existing models for excess base current caused by radiation were derived using established Shockley-Read-Hall (SRH) surface recombination statistics, which are directly proportional to surface carrier concentration. In these models the capacity of interface traps to alter the number of surface carriers at the LPNP base region was acknowledged, but not incorporated.

At the LPNP base surface, carrier concentration depends on the surface potential. Therefore, to determine how the charged interface traps alter effect the radiation-induced LPNP base current response, it was critical to develop a method of accurately calculating base surface potential. To achieve this calculation, it was proposed to use the standard MOS surface potential model. The MOS surface potential was derived in detail, and modifications were proposed to make the model suitable for calculating the base surface potential of a basic LPNP and a LPNP with a metal field plate deposited over the oxide layer and emitter contact. Surface potential values were obtained numerically using iterative MATLAB functions given inputs interface trap concentration, trapped oxide charge concentration, and emitter voltage. The MATLAB calculations of the implicitly defined surface potential values were shown to accurately match the LPNP TCAD device simulations of base surface potential simulated with same inputs.

The improved model presented in this thesis quantifies the impact of charged interface trap defects on the surface potential and carrier concentration at the bipolar base surface. It incorporates the numerically solved surface potential results from the modified

MOS model, as well as the impact of emitter-base series resistance, into the existing model for excess base current. The result is such that by capturing the electrostatic effects of charged interface traps and series resistance, the improved model provides a much closer match to both the excess base current vs emitter voltage and excess base current vs. interface trap concentration response obtained from TCAD simulations on a representative LPNP field-plated LPNP BJT structure. These more accurate models of TID as well as low dose rate effects in BJTs can support faster and lower cost qualification of linear bipolar COTS components for use in space systems

An experiment was can conducted in which National Semiconductor (NSC) fabricated gated LPNP (GLPNP) devices were exposed to various levels of total ionizing doses (TID) at different does rates for a fixed transistor bias. The intent of the experiment was to investigate the effect of ambient hydrogen concentration on the TID response versus dose rate in linear bipolar circuits [8]. Although the correlation between hydrogen levels and dose rate effects is not the focus in this thesis, the experiment provided data relating interface trap concentrations and excess base current exhibited in the GLPNP transistors. The existing and improved models are plotted against the experimentally obtained excess base current data versus interface trap concentration. The improved model shows a closer match than the existing model to the experimental excess base current data at each interface trap concentration. Although this is positive result that further confirms the effectiveness of the improved model in predicting the excess base current response in irradiated PNP transistors, it should be noted that the extraction techniques used to determine defect concentrations are often imprecise. Furthermore the exact physical dimensions and doping profiles of the irradiated device are only approximated in the model calculations.

Therefore, to confirm with absolute certainty the accuracy of the improved model, more exact physical details of the device under test are necessary. As such, the ability of the improved model to accurately predict excess base current responses was primarily verified through TCAD device simulation where precise device parameters and radiation-induced defect levels can be defined.

REFERENCES

[1] D. R. Ball, R. D. Schrimpf, and H. J. Barnaby, "Separation of ionization and displacement damage using gate-controlled lateral PNP bipolar transistors," Nuclear Science, IEEE Transactions on, vol. 49, pp. 3185-3190, 2002.

[2] H. J. Barnaby, S. K. Smith, R. D. Schrimpf, D. M. Fleetwood, and R. L. Pease, "Analytical model for proton radiation effects in bipolar devices," *IEEE Transactions on Nuclear Science*, vol. 49, pp. 2643-2649, 2002.

[3] R. L. Pease, D. G. Platteter, G. W. Dunham, J. E. Seiler, H. J. Barnaby, R. D. Schrimpf, *et al.*, "Characterization of enhanced low dose rate sensitivity (ELDRS) effects using gated lateral PNP transistor structures," *IEEE Trans Nucl. Sci.*, vol. 51, p. 3773, 2004.

[4] S. L. Kosier, R. D. Schrimpf, D. M. Fleetwood, M. DeLaus, R. L. Pease, W. E. Combs, et al., "Charge Separation for Bipolar Transistors," *IEEE Trans. Nucl. Sci*., vol. 40, pp. 1276-1285, 1993.

[5] H. J. Barnaby, B. Vermeire, and M. J. Campola, "Improved model for increased surface recombination current in irradiated bipolar junction transistors," *IEEE Trans. Nucl. Sci.*, vol. 62, pp. 1658 - 1664, 2015.

[6] Analog Devices datasheet, http://www.analog.com/media/en/technical-documentation/data-sheets/AD590.pdf

[7] H. J. Barnaby, R. D. Schrimpf, D. M. Fleetwood, and S. L. Kosier, "The effects of emitter-tied field plates on lateral PNP ionizing radiation response," in *Bipolar/BiCMOS Circuits and Technology Meeting, 1998. Proceedings of the 1998*, 1998, pp. 35-38.

[8] R. L. Pease, P. C. Adell, B. G. Rax, X. J. Chen, H. J. Barnaby, K. E. Holbert, and H. P. Hjalmarson, "The effects of hydrogen on the enhanced low dose rate sensitivity (ELDRS) of bipolar linear circuits," *IEEE Trans. Nucl. Sci.*, no. 6, pp. 3169–3173, Dec. 2008.

[9] Texas Instruments website, http://www.ti.com/product/LM139 and datasheet, http:www.ti.com/lit/ds/symlink/lm139.pdf

[10] D. M. Schmidt, A. Wu, R. D. Schrimpf, D. M. Fleetwood, and R. L. Pease, "Modeling ionizing radiation induced gain degradation of the lateral pnp bipolar junction transistor," IEEE Trans. Nucl. Sci., vol. 43, pp. 3032-3039, 1996.

[11] Silvaco, Inc ATLAS user manual, http://ridl.cfd.rit.edu/products/manuals/Silvaco/atlas_users.pdf

[12] D. A. Neaman, *Semiconductor Physics and Devices-Basic Principles*. Boston: Irwin, 1992.

[13] Y. Taur and T. H. Ning, *Modern VLSI Devices*. New York: Cambridge Univ. Press, 1998.

[14] R. S. Muller and T. I. Kamins, Device Electronics for Integrated Circuits, Second ed. New York: Wiley, 1986.

[15] I. S. Esqueda, H. J. Barnaby, and P. C. Adell, "Modeling the Effects of Hydrogen on the Mechanisms of Dose Rate Sensitivity," *IEEE Transactions on Nuclear Science*, vol. 59, pp. 701-706, 2012.

[16] X. J. Chen, H. J. Barnaby, B. Vermeire, K. Holbert, D. Wright, R. L. Pease, *et al.*, "Mechanisms of enhanced radiation-induced degradation due to excess molecular hydrogen in bipolar oxides," *IEEE Trans Nucl. Sci.*, vol. 54, pp. 1913-1919, 2007.

[17] I. Sanchez Esqueda, H. J. Barnaby, and M. P. King "Compact Modeling of Total Ionizing Dose and Aging Effects in MOS Technologies," *IEEE Transactions on Nuclear Science*, vol. 62. pp. 1501-1515, 2015

[18] R. F. Pierret, *Advanced Semiconductor Fundementals* vol. 4. Reading, Massachusetts: Addison-Wesley, 1987.

[19] P. J. McWhorter and P. S. Winokur, "Simple technique for separating the effects of interface traps and trapped-oxide charge in metal-oxide-semiconductor field-effect transistors," *Appl. Phys. Lett.*, vol. 48, pp. 133-135, 1986.

[20] T. L. Chen and G. Gildenblat, "Analytical approximation for the MOSFET surface potential," *Solid-State Electron.*, vol. 45, pp. 335–339, 2000.

[21] G. Gildenblat, W. Hailing, C. Ten-Lon, G. Xin, and C. Xiaowen,"SP: An advanced surface potential-based compact MOSFET model,"*IEEE J. Solid-State Circuits*, vol. 39, pp. 1394–1406, 2004.

[22] MathWorks, Inc website, https://www.mathworks.com/help/matlab/ref/fzero.html